



UNIVERSITY OF
LIVERPOOL

Surface Analysis of the Ag-In-Yb 1/1 Quasicrystal Approximant

Kai McGilligan Oliver - 200640062

Dissertation Project – Masters of Physics F303

2011-2012

Project Supervisor:
Dr H. R. Sharma

Abstract

This report investigates the arrangement of atoms and the crystal planes likely to be exposed on a single-grain, [100] bulk-terminated Ag-In-Yb 1/1 quasicrystal approximant. Of the two families of quasicrystalline alloys, icosahedral quasicrystals (QCs) have been of particular scientific interest since the discovery of stable binary samples. *i*-Cd-Yb is renowned for having its exact atomic positions modelled through a comparison of X-ray diffraction patterns with the structure of closely related crystals – called approximants. Sample surface preparation techniques (such as high temperature annealing) in vacuums of the order 10^{-10} mbar are unsuitable for use on alloys containing Cd due to its high vapour pressure. Isostructural QCs, for example *i*-Ag-In-Yb and their approximants, can be prepared in such conditions and studied by means of LEED (low energy electron diffraction) and STM (scanning tunnelling microscopy). Previous studies of XRD patterns (X-ray diffraction) have provided a well-proven computer model of the bulk atomic structure of the Ag-In-Yb approximant. This study indicated intermediate-density terrace step-heights of 2.77 Å and 2.47 Å, and a departure from the predicted bcc Tsai cluster lattice in the form of rectangular unit cells: the parameters of which were $a_x = 13.23$ Å and $a_y = 15.42$ Å. It is believed that the off-centre rectangular unit belongs to the high density plane A/A'. Thermal drift of the sample has been ruled out of being responsible for this unusual observation, as has large-scale surface reconstruction. LEED suggests these planes are in the minority as a square reciprocal space lattice is observed. Future research into ridged intermediate planes by associated research teams is proposed as the next step for confirmation of the model.

List of Figures, Tables and Graphs

<i>Figure 1</i>	Diffraction through a slit	<i>Figure 24</i>	Unusable Data example 1
<i>Figure 2</i>	Ewald sphere	<i>Figure 25</i>	Unusable Data example 2
<i>Figure 3</i>	Tessellating Tiles	<i>Figure 26</i>	Unusable Data example 3
<i>Figure 4</i>	Quasiperiodicity in 1-dim	<i>Figure 27</i>	Unusable Data example 4
<i>Figure 5</i>	Penrose tiling	<i>Figure 28</i>	Unusable Data example 5
Figure 6	i-Ag-In-Yb fivefold surface	<i>Figure 29</i>	FFT
<i>Figure 7</i>	Phason flipping	<i>Figure 30</i>	Self-correlation
<i>Figure 8</i>	Approximation of an irrational slope	<i>Figure 31</i>	Histogram method
<i>Figure 9</i>	Periodic table	Figure 32	Proposed Ridged model
Figure 10	Shimoda Model 1	<i>Figure 33</i>	Planar Crust
Figure 11	Shimoda Model 2	<i>Figure 34</i>	A/A' plane rectangular unit cell
<i>Figure 12</i>	RT-STM Chamber	<i>Figure 35</i>	Cluster resolution of terrace steps
<i>Figure 13</i>	LEED apparatus	<i>Figure 36</i>	Atomic resolution 1
<i>Figure 14 a</i>	(111) plane of fcc lattice	<i>Figure 37</i>	A/A' plane segment
<i>Figure 14 b</i>	(100) plane of bcc lattice	<i>Figure 38</i>	Atomic resolution2
<i>Figure 14 c</i>	Diffraction directions in Cu(111)	<i>Figure 39</i>	Approximant sample of sample plate
<i>Figure 15</i>	LEED Cu(111) calibration	<i>Figure 40</i>	Mounting approximant sample
<i>Figure 16</i>	LEED approximant data	Table 1	Shimoda Model predictions
Figure 17	STM	Table 2	Omicron SpectraLEED specifications
<i>Figure 18</i>	RT-STM	Table 3	Omicron STM specifications
Figure 19	Gwyddion information panel	Table 4	Example data sets
<i>Figure 20</i>	Proximity groups	Graph 1	"Frequency of Average Step Heights Across 132 Steps/ 16 images"
<i>Figure 21</i>	STM data; prox' group	Graph 2	Histogram S1
<i>Figure 22</i>	Plane filtered STM image of terraces	Graph 3	Histogram S2
Figure 23	WSxM toolbar	Graph 4	Gaussian curve fitted to peaks in step heights

All Figures, Tables and Graphs are property of the University of Liverpool: Exceptions below.

<i>Figure 6</i>	Sharma et al " <i>Structure of the fivefold surface of the Ag-In-Yb icosahedral quasicrystal</i> " (2009)
<i>Figure 10</i>	Tohoku University / NIMS (2011)
<i>Figure 11</i>	Tohoku University / NIMS (2011)
<i>Figure 17</i>	(2012) http://www.iap.tuwien.ac.at/www/surface/stm_gallery/stm_schematic
<i>Figure 19</i>	Gwyddion, (2012)
<i>Figure 23</i>	WSxM (2012)
<i>Figure 32</i>	Tohoku University / NIMS (2011)
Table 1	Tohoku University / NIMS (2011)
Table 2	Omicron NanoTechnology (2003)
Table 3	Omicron NanoTechnology (2003)

ABSTRACT	2
LIST OF FIGURES, TABLES, AND GRAPHS	3
1. INTRODUCTION	6
2. QUASICRYSTALS: THE FUNDAMENTALS	9
2.1.1. <i>THE BRAVAIS LATTICE</i>	9
2.1.2. <i>ATOMIC PLANES AND MILLER INDICES</i>	9
2.1.3. <i>THE BASIS</i>	11
2.1.4. <i>THE RECIPROCAL LATTICE AND BRAGG DIFFRACTION</i>	11
2.1.5. <i>FORBIDDEN SYMMETRIES</i>	16
2.1.5. <i>EXTRA DIMENSIONS AND QUASI-ORDER</i>	17
3. QUASICRYSTALS AND APPROXIMANTS	20
3.1.1. <i>CLUSTERS AND PLANES</i>	21
3.1.2. <i>PHASON FLIPS</i>	22
3.1.3. <i>QUASICRYSTAL APPROXIMANTS</i>	24
3.1.4. <i>TSAI CLUSTERS IN i-CD-YB</i>	25
3.2.1. THE “SHIMODA” MODEL.....	26
3.2.2. PREDICTIONS FOR THE STRUCTURE OF 1/1 AG-IN-YB	29
4. EXPERIMENT ONE: LEED	30
4.1. <i>SURFACE PREPARATION</i>	30
4.2.1. <i>LOW ENERGY ELECTRON DIFFRACTION</i>	31
4.2.2. <i>LEED APPARATUS</i>	32
4.2.3. LEED ANALYSIS OF AG-IN-YB	24
4.2.4. LEED RESULTS AND DISCUSSION	37
4.2.5. SUMMARY	39
5. EXPERIMENT TWO: STM	40
5.1.1. <i>SCANNING TUNNELLING MICROSCOPY</i>	40
5.2.1. DATA ANALYSIS: AIMS AND HYPOTHESIS.....	41
5.2.2. <i>ORIGIN OF DATA</i>	42
5.2.3. <i>RELATED AND UNRELATED DATA</i>	44
5.2.4. <i>SPM SOFTWARE</i>	47
5.3. PROCESS OF IMAGE ANALYSIS.	48
5.3.1. <i>UNUSABLE DATA</i>	49

5.3.2. <i>FILTERING STM IMAGES</i>	50
5.3.3. <i>TERRACE STEP HEIGHT AND UNIT CELL LATTICE VECTORS</i>	51
5.4. STEP HEIGHT	53
5.4.1. HISTOGRAM / RESULTS	54
5.4.2. <i>DISCUSSION OF RIDGED TERRACES</i>	56
5.4.3. <i>ERROR ANALYSIS</i>	57
5.4.4. SUMMARY	58
5.5. CLUSTER SPACING	60
5.5.1. <i>MEASURING X AND Y LATTICE COMPONENTS</i>	60
5.5.2. RESULTS	61
5.5.3. <i>CLUSTER RESOLUTION OF TERRACE SITES</i>	63
5.5.4. <i>ATOMIC RESOLUTION</i>	64
5.5.5. SUMMARY	66
6. CONCLUSION AND FUTURE RESEARCH	67
7. BIBLIOGRAPHY	69
8. APPENDIX 1	71
9. APPENDIX 2	77

1. Introduction

2011 saw the prestigious Nobel Prize in Chemistry awarded to Israeli Professor Dan Shechtman for his discovery of the quasiperiodic, or quasicrystalline, structure in aluminium-based metal alloys. (R.Noorden, 5th Oct 2011) The accolade gave distinguished acknowledgement to the rapidly growing study of these so-called quasicrystals (*QCs*). Shechtman's *QC* was artificially composed of $\text{Al}_{86}\text{-Mn}_{14}$ (subscript indicating percentage of composition) and grown via rapid cooling of a melt-phase. The icosahedral phase produced possessed no periodicity, however retained perfect long-range order. The former is supported by the existence of 10-fold symmetries found in electron diffraction patterns, while the latter was proven by sharp, intense Bragg peaks from the constructive interference of diffracted electron beams. (Shechtman, et al., 1984)

Within the international crystallography community *QCs* have caused a lot of commotion surrounding the new physical phenomena discovered in certain alloys. Shechtman was met with derision from all scientific fronts for his claim to have found a new class of solid that breaks many of crystallography's long-established laws; this included scorn from the two-times Nobel Prize winner Linus Pauling. Yet now, more than 30 years later on and hundreds of quasicrystals have since been discovered. It seems now all that opposition has faded sheepishly into the past.

Although metallic, *QCs* do not behave like metals: the way in which the electrons are confined within atomic clusters makes them poor conductors of heat and electricity. They also have incredibly low friction coefficients in non-lubricated conditions, and multi-pass tests liken the coefficient to diamond planes gliding over each other. (Dubois, 2002) Still, the fundamental effect of quasiperiodic structure on a material's properties remains truly uncharted territory.

Surfaces behave differently to the bulk material, thus are responsible for different phenomena. For example: the work function ϕ , normally thought of as a bulk property, is determined as a consequence of surface dipole layers. In the bulk electrons cannot escape through the surface without being given enough energy to penetrate the dipole layers. (Attard & Barnes, 1998) It is also observed universally that the termination of the bulk in crystals causes reconstruction of the atoms at and near the surface due to the relaxing of interatomic forces.

Appreciation of the surface of QC materials is therefore very important in identifying the influence of quasicrystallinity. Efforts to simplify the study of quasicrystallinity have been made in epitaxial experiments which have built quasicrystalline layers of single-element atoms using QCs as substrates. Monolayer depositions of Bi and Sb grown on QC become quasiperiodic; opening up the potential to study QC structures without the impact of complex alloy atomic composition. The only drawback to QC monolayers was that they could not be made into bulk structures and retain their quasiperiodicity. This is because of the weak atomic forces between successive layers and the need for the layer coverage to minimise energy. (Franke & Berlin, 2003)

Where else then can we look simple quasiperiodic structures? Many stable QCs that are tertiary (compose of three elements) are still very complex. However the simpler binary (two elements) icosahedral QC phase was discovered in the *i*-Cd-Yb alloy, and subsequently its atomic structure was modelled using a combination of conventional band theory and XRD (X-ray diffraction) data. (Takakura, et al., 2007) This was an exceptional feat, and gave QC surface researchers a new opportunity to pursue surface characterisation. However *i*-Cd-Yb cannot be examined under UHV due to high vapour pressure of Cd which causes evaporation during heating. An isostructural counterpart, *i*-Ag-In-Yb emerged as a solution to the heating problem as both Ag and In are stable under UHV. Thus studies of this surface are relevant to evaluate the surface qualities of a whole family of quasicrystals.

A number of interfaces studies already exist on *i*-Ag-In-Yb, (Sharma, et al., 2009)(Sharma, et al., 2010)(Nugent, et al., 2010)(Nugent, et al., 2011) but virtually no surface analysis exists for its closely related counterpart, the bcc structured Ag-In-Yb. This is an approximant of *i*-Ag-In-Yb: sharing the same chemical composition as the QC however preserving a crystalline form. A periodic system is far easier to investigate, and for researchers, studies of the approximant can give an insight into the real differences between ordered and quasi-ordered solids.

For this project, two approximant Ag-In-Yb samples grown and cut by Tohoku University in Japan (collaborating with the National Institute of Material Science) were provided for scanning probe microscopy and electron diffraction examination. The quality of these samples is thus far unprecedented due to the achievement of single-grain specimens. The fundamental objective of the project was to use experimental data and a structural model provided by Tohoku University to determine the unit cell vectors of the [100] surface and

identify terraces formed on approximant exterior. The report will begin with some key concepts in crystallography and an explanation of how quasicrystals possess forbidden symmetries. Our definition of a QC approximant is made geometrically within external and internal subspaces, so to highlight the relationship between 2-dim periodic and quasiperiodic structures. The 3-dim model of the atomic structure is contained within an *IGOR Pro* software module: its predictions are herein discussed. Following this is a detailed insight into the preparation of samples for use in ultrahigh vacuum systems: the decision to expand lab notes into an essay format was made so to provide any future experimenters at the University of Liverpool with touchstone material to refer to, as well as to contextualise the processes of polishing, mounting, sputtering and annealing. Then the physical principles of the low energy electron diffraction (LEED) and scanning tunnelling microscope techniques (STM), and their suitability for surface analysis, will be explored.

K-vector data compiled from LEED images of the Ag-In-Yb approximant will include a comparison with Cu(111) data for calibration of the LEED screen, then comparison using IGOR software will be shown to confirm the predicted real lattice vectors. Height maps obtained from STM imaging will give accurate pictures (the smallest image axes reaching a scale of tens of nanometres) of terraces on the sample surface and the atomic structure can be found when comparing against the bulk structure of modelled Ag-In-Yb. And while STM image analysis is a topic of great depth and breadth, a suitably basic guide to quality assessment and filtering techniques using *Windows Scanning x Microscope* (WSxM) and *Gwyddion* software is presented.

STM data had to be collected from another source when a key component of the UHV chamber could not be used, so no STM methodology is included in the report. It was hoped that analysis of thin film growth of Pb to form quasicrystalline structures could occur during the project using the Auger electron spectroscopy system; however the project ran into a number of problems, so Pb epitaxial growth was not a viable option. In light of these trials, an analysis and comparison of various STM images to the model has still been completed. The qualitative nature of the resulting data set means that quantifying error due to thermal drift of the sample, piezo-electric creep, or STM calibration, becomes somewhat redundant: the reasons why are noted. The report will conclude by identifying areas of improvement and further study.

2. QUASICRYSTALS: THE FUNDAMENTALS

What is a quasicrystalline phase? What is an approximant? To answer these questions, we must first understand how atoms fill space in condensed matter states. Crystalline solids exhibit varying degrees of hardness, density, transparency, conductivity and diffusion that result directly from the nature of bonds and periodic arrangement of its constituent atoms. From the necessity to understand these properties was borne a mathematical illustration of the atomic arrangement, steeped in the understanding of allowed and forbidden symmetries.(Stadnik, 1999) This section will expand upon a few key crystallography concepts, as well as explaining the principle behind electron diffraction.

2.1.1 THE BRAVAIS LATTICE

The atoms in a ‘perfect’ crystal can be associated with an infinite three-dimensional (3-dim) array of points, where each point is treated as identical to its neighbours (i.e. a **lattice**). By giving the points an indistinguishable nature it would be observed that moving from one lattice point to another does not change the appearance of the lattice, and thus we say that the lattice has perfect translational symmetry. If we choose an arbitrary origin, any other lattice point will have the position vector:

$$\mathbf{r} = n_1\mathbf{a} + n_2\mathbf{b} + n_3\mathbf{c}$$

Equation 1

Here, the vector coefficients n_i are integers, while **a**, **b**, **c** are known as primitive vectors, so called for they fundamentally decide the form of translational symmetry that the lattice will adopt. In reality there are only 14 different periodic ways of forming a lattice from the primitive vectors, and these arrays are called **Bravais lattices**.(Attard & Barnes, 1998) The smallest volume unit that contains information to describe the whole lattice is called a **unit cell**. Despite only containing a few points, the unit cell will accurately describe the lattice when replicated to infinity.

2.1.2 ATOMIC PLANES AND MILLER INDICES

To further enhance the crystallographer’s vocabulary, **Miller indices** were introduced to denote planar direction in the Bravais lattice. The lattice may be considered not only as a boundless tessellation of unit cells but also as a stacking of 2-dim arrays. There are an infinite

number of these **planes** of points, organised into an infinite number of **families**. A family is a collection of parallel planes sharing the same primitive vectors. The families are characterised by the arrangement of points, density of points, and the spacing between planes (interplanar spacing increases with greater density).

The rules for deriving Miller indices are as follows:

- Determine the intercepts of the plane along the crystallographic axes, in terms of unit cell dimensions: i.e.

$$\frac{x}{|a|}, \frac{y}{|b|}, \frac{z}{|c|}$$

- Take the reciprocals: i.e.

$$\frac{|a|}{x}, \frac{|b|}{y}, \frac{|c|}{z}$$

- Write the reciprocals in the form of integers, so that their lowest common denominator is 1.
- The generic form of the Miller index is then denoted by (hkl) .

It can be shown without much effort that if the x, y, z intercepts are 1, 2, and 3 in terms of the unit cell dimensions, the Miller indices are calculated as $(hkl) = (632)$. The smaller the Miller index is, the closer the associated plane is to being parallel to the axis, whereas the larger the index the closer it is to being perpendicular.

Some further observations: *a)* multiplying or dividing a Miller index by a constant has no effect of the orientation of the plan, *b)* if a plane is parallel to an axis, its intercept is at infinity and its Miller index is zero, *c)* if a plane has negative intercept, such that the plane slopes with a negative gradient component, the negative number is denoted by a bar above the number. It is erroneous to change the sign through division or multiplication when deriving a Miller index, as this implies symmetry that the crystal may not have. For example, do not divide $(\bar{1}\bar{1}\bar{1})$ by -1 to get (111)

Use of Miller indices removes the complication of dealing with infinite planar intercepts. Also, specifying dimensions in unit cell terms means that the same label can be applied to any plane with a similar stacking pattern, regardless of the way the unit cell repeats itself. (111) lattice planes will always ‘step’ the same way regardless of the type of crystal.

Other forms of the Miller notation include $[hkl]$ and $\langle hkl \rangle$: with square instead of round brackets denoting a direction in normal to the plane indices; and similarly, the chevron parenthesis represents the family of all directions that are equivalent to $[hkl]$ by symmetry.

2.1.3. THE BASIS

Associated with the Bravais lattice are the physical sites of the atoms themselves. The atomic positions are captured on the Bravais ‘netting’, like a fisherman casting a vast net out into a sea of fish. For most crystals a shoal of atoms is caught by each lattice point, although simpler crystals (e.g. copper) will only have one atom per lattice point. This group of atoms associated with each point is called a **basis**. We can identify the atomic positions with the vector:

$$\mathbf{r}_j = n_1\mathbf{a} + n_2\mathbf{b} + n_3\mathbf{c} + \mathbf{R}_j$$

Equation 2

Here, \mathbf{R}_j denotes the position of the atom j with respect to the Bravais lattice point.

The basis is limited by symmetry however, much like the lattice. If the structure is to remain periodic on a short order scale, we must now account for the atomic arrangement being able to transform into an image of itself under rotational and reflection transformations. The possible combinations of transformations in 3-dim, whilst numerous, are constrained to the 230 operations termed **space groups**. Space groups won’t be discussed in detail in this report but for further reading W. M. Meier provides an uncomplicated 3-dim appraisal of space group theory (Meier, 1984).

We now have the two ingredients required to describe the atomic form of any perfectly periodic structure. Note that in practise crystalline structures contain many unwanted defects that are ignored when dealing with the ideal case.

2.1.4. THE RECIPROCAL LATTICE AND BRAGG DIFFRACTION

How can we confirm whether crystals adhere to this description of lattice and basis? The invention of X-ray, electron and neutron scattering experimentation proved to be a vital set of tools to determine bulk and surface crystal structure that are continued in their use today.

Electron interactions with the target crystal differ from X-ray and neutron beam interactions, and each is useful for delving into different properties. The electron form factor takes into

account elastic electron cloud scattering and elastic nuclear scattering. Because of their strong interaction with matter they penetrate only a few atomic layers deep into sample the before being scattered, making electrons particularly useful for surface studies.

The diffraction experiments take advantage of the long range order of crystalline solids, and the back-scattered interference pattern produced from a crystal sample placed in the path of a ray of energetic particles or high-frequency light. De Broglie's concept of wave-particle duality explains why we can use particles to acquire diffraction patterns, providing they are of small enough wavelength. This is known as Bragg diffraction, and the pattern of intensity peaks they produce are representations of **reciprocal lattices**.

The direction normal to a family of crystal planes, $[hkl]$ can be written as a unit vector \mathbf{n}_{hkl} . We also know that the family of planes are separated by an interplanar distance d_{hkl} . Defined by these parameters, the set of vectors:

$$\mathbf{G}_{hkl} = 2\pi \frac{\mathbf{n}_{hkl}}{d_{hkl}}$$

Equation 3

define the reciprocal space, which we will further explain presently.

\mathbf{G}_{hkl} can be thought of as a vector that ends on a point of the reciprocal lattice. Thus \mathbf{G}_{hkl} can be described in another form:

$$\mathbf{G}_{hkl} = h\mathbf{a}^* + k\mathbf{b}^* + l\mathbf{c}^*$$

Equation 4

where $\mathbf{a}^* \mathbf{b}^* \mathbf{c}^*$ are vectors related to the real space lattice $\mathbf{r} = n_1\mathbf{a} + n_2\mathbf{b} + n_3\mathbf{c}$ by:

$$\mathbf{a}^* = 2\pi \frac{\mathbf{b} \times \mathbf{c}}{\mathbf{a} \cdot (\mathbf{b} \times \mathbf{c})} \quad \mathbf{b}^* = 2\pi \frac{\mathbf{c} \times \mathbf{a}}{\mathbf{a} \cdot (\mathbf{b} \times \mathbf{c})} \quad \mathbf{c}^* = 2\pi \frac{\mathbf{a} \times \mathbf{b}}{\mathbf{a} \cdot (\mathbf{b} \times \mathbf{c})}$$

Equation 5

and simplified in the case of the scalar triple product:

$$\mathbf{a}^* \cdot \mathbf{a} = 2\pi \quad \dots etc \dots$$

Equation 6

Reciprocal lattices vectors exist in reciprocal space, or k-space. K-space refers to a collection of \mathbf{k} wave vectors in their own vector space. The solution to Schrödinger's equation is a plane

wave (or a wave-like particle) with $\Psi = Ae^{i(\mathbf{k}\cdot\mathbf{r}-\omega t)}$, containing the wave vector that denotes the direction of the incident wave. Traditionally in wave mechanics the propagation of a plane wave adheres to the Huygens-Fresnel principle: the rectilinear propagation of a wave arises from the initial wave front comprising of point sources of secondary spherical waves. In the classic single slit experiment the wave front is strongly diffracted when the slit size is comparable to that of the wavelength; a larger slit will diffract much less effectively, while a slit that is too small will act as a reflective surface. (See Figure 1)

The diffraction of electrons from a surface can be considered as waves impinging upon a grid of atoms. The atoms act like re-emitting point sources through an elastic transfer of energy (with no change in wavelength of the beam) whereby the beam energy and atomic characteristics affect the angle and intensity of the diffracted electrons.

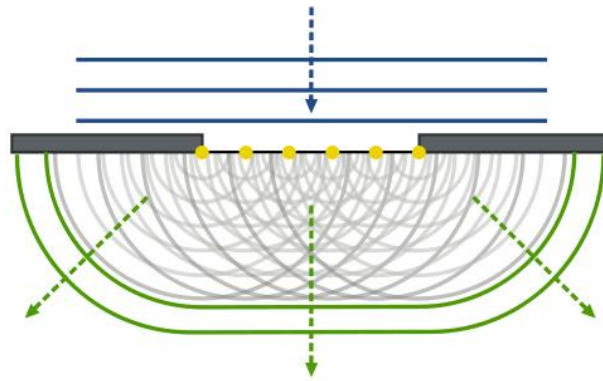


Figure 1 : A wave approaches an aperture of a width comparable to the wavelength of the wave: point like radiations simulate the progression of the resulting diffraction.

At a point far from the crystal, the condition for constructive interference of the diffracted waves is:

$$a \sin(\theta_i) = n\lambda$$

Equation 7

where θ_i is the incident angle, (normal to the surface), a is the lattice constant, n is an integer, and λ is the wavelength of light. Recall that the incident wave has a wave vector \mathbf{k} : when scattered by the family of identical planes of atoms it encounters, the outgoing wave changes in direction but not in magnitude, i.e. $\mathbf{k} \neq \mathbf{k}'$ but $|\mathbf{k}| = |\mathbf{k}'|$.

Also we know that the wavelength does not change in an elastic collision, and this can be represented by $|\mathbf{k}| = |\mathbf{k}'| = 2\pi/\lambda$. Taking this definition of the magnitude of \mathbf{k} we can substitute into the Eq.7 to get:

$$a \sin(\theta_i) = n \frac{2\pi}{|\mathbf{k}|}$$

Equation 8

$$|\mathbf{k}| \sin(\theta_i) = n \left(\frac{2\pi}{a} \right)$$

Equation 9

$|\mathbf{k}| \sin(\theta_i)$ is the component of the momentum vector parallel to the surface, which we can label $\mathbf{k}_{||}$. The right hand side of the equation is the magnitude of the reciprocal lattice vector. Note that this can only take discrete values due to the constraint of the integer values of n . The parallel momentum of the incident electron is exchanged with the surface in quantised units, providing us with a way of denoting the scattering effect, i.e. the change in the incident and outgoing waves is:

$$\Delta \mathbf{k}_{||} = \mathbf{k}'_{||} - \mathbf{k}_{||}$$

Equation 10

In order for constructive interference to be observed, $\Delta \mathbf{k}$ must belong to the reciprocal lattice vector \mathbf{G}_{hkl} so that:

$$\begin{aligned} \Delta \mathbf{k} &= \mathbf{G}_{hkl} \\ &= h \left(\frac{2\pi}{\mathbf{a}} \right) + k \left(\frac{2\pi}{\mathbf{b}} \right) + l \left(\frac{2\pi}{\mathbf{c}} \right) \\ &= h\mathbf{a}^* + k\mathbf{b}^* + l\mathbf{c}^* \end{aligned}$$

Equation 11

The scattering event can therefore be drawn in k-space. Consider the 2-dim k-space diagram in Figure 2. The vertical lines intersecting the x axis are the reciprocal lattice rods, which are separated by $2\pi/|\mathbf{a}|$ where $|\mathbf{a}|$ is the nearest-neighbour atomic distance. The sample is positioned so its surface is orientated with respect to the x axis. To decide the starting point of the incident wave vector \mathbf{k} , a point A associated with the orientation of the sample is chosen. The location of A is governed by the length of \mathbf{k} and the incident angle θ_i . The end of \mathbf{k} is

then positioned at the origin. The circle crossing through the reciprocal rods is drawn using A as its circle centre. Ewald's circle (more commonly known as the Ewald's sphere in 3-dim) demonstrates the fulfilment of the diffraction condition Eq.7 at the point of intersection of the circle and the rod.

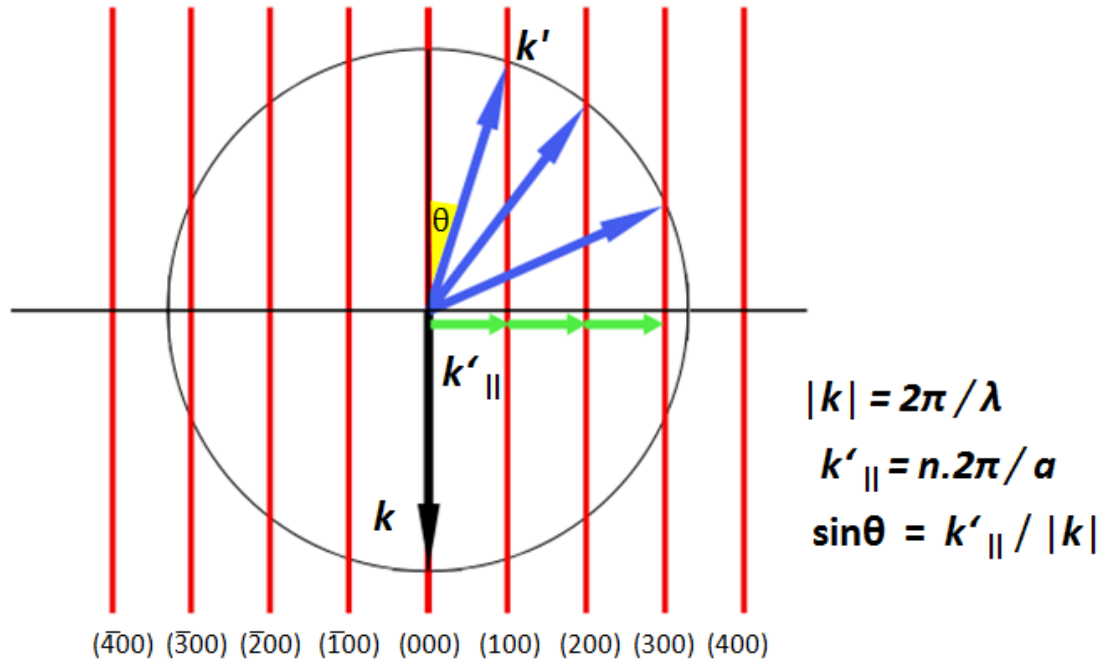


Figure 2: The Ewald sphere in 2-dim shows the incident wave vector as the radius of a circle that intersects the reciprocal lattice rods. Every time the circle intersects a rod, constructive diffraction peaks are produced. Any intersections below the central line occur in the solid, thus do not appear. The rods are spaced in reciprocal lattice vector units, where a is the real space lattice constant. The angle in real space θ_i is equivalent to the angle to normal of the surface θ , which can be found through the equations above.

This means we can represent the possible \mathbf{k}' vectors as arrows that end at these intersections. In the case of the incident wave vector approaching normal to the surface, ($\theta_i = 0$) then:

$$\Delta\mathbf{k}_{||} = \mathbf{G}_{hkl||} = \mathbf{k}'_{||}$$

Equation 12

This is the condition for diffraction. \mathbf{k}' must have quantised parallel components for Bragg diffraction to occur. We see thus that although energy is conserved in the elastic diffraction process, if a \mathbf{G}_{hkl} vector is exchanged with the surface, the incident wave / particle must undergo a quantised change in direction to preserve momentum. For constructive Bragg peaks to be realised, Eq.12 must be satisfied.

2.1.5 FORBIDDEN SYMMETRIES.

Earlier in this chapter we stated that the crystal basis is subject to a set of symmetry laws. Outside of the 230 space groups that exist, there can be no 3-dim periodic crystalline structures. Let us take a 2-dim approach that will infer rules implicit in 3-dim symmetry: an infinite plane of lattice points could be thought of as a collection of tiles all slotted next to each other, where on the vertices of the tile lie the points.

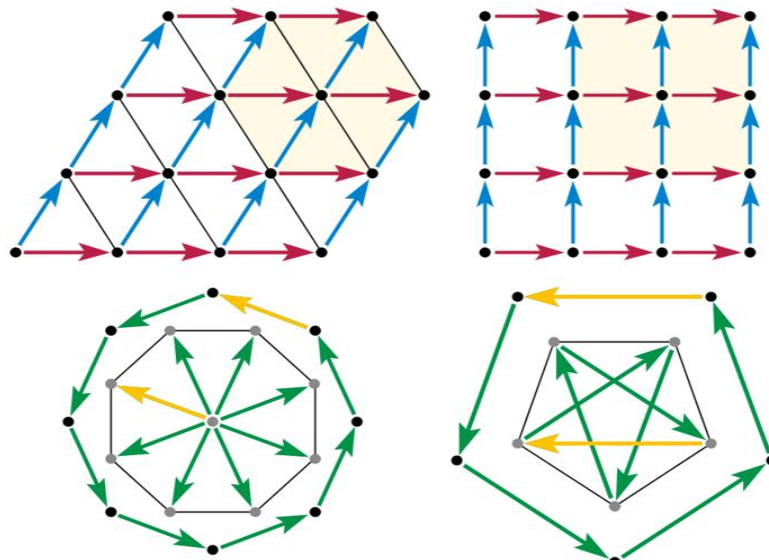


Figure 3: Examples of allowed (top: 3 fold and 4 fold symmetry) and forbidden (8-fold, 5-fold) tessellating tiles. The alternating coloured arrows show that although the top tilings have translational symmetry, the bottom two cannot possess this quality.

The tessellation of tiles mirrors the repeating unit cell volume of a crystal lattice – a tile's vertices must share a point between other tiles if the plane is to be filled completely by the tiles, just as in the atomic case. Tessellation of polygons strictly limits the vertex angle to an integral fraction of 2π . Triangles, squares and hexagons obviously exhibit this property, and can be said to have three-, four-, and six-fold rotational symmetry, respectively. (In addition, two-fold symmetry is also contained in a square tile, and a hexagon tile has two- and four-fold as well.) Conversely, five-folded and greater than six-folded tile symmetries cannot fill 2-dim space without leaving gaps or having the tiles overlap (see Figure 3). The regular polygons with these forbidden symmetries have vertex angles that do not wholly fit into 2π ; e.g. a pentagon vertex angle of $2\pi/(3.333\dots)$. More generally, tessellation will only occur for n -sided polygons if $2n/(n - 2)$ is an integer.

Moving on from 2-dim, it is not hard to envisage that similar restrictions apply to a 3-dim periodic lattice: if you were to throw a set of dodecahedron into a box, the way they fall will always leave gaps in the stack. Space groups were thought to define all crystalline matter by way of allowed symmetries.

2.1.6 EXTRA DIMENSIONS AND QUASI-ORDER

The following section is a meaningful step towards explaining why quasicrystals do not possess translational periodicity but do display long range order. The former is manifested in the presence of a non-crystallographic rotational symmetry and the latter in the occurrence of sharp diffraction spots.

Amorphous and structurally disordered materials (i.e. metallic glass) are difficult to characterise using diffraction methods. Amorphous scattering is weak compared to that of a crystalline solid, and is spread throughout reciprocal space instead of being concentrated into a few sharp Bragg peaks. (Zallen, 1998) The detailed level of analysis to acquire real-space data is also much more involved for amorphous samples as they have no long-range order. Their systems may contain many similar regions, which might be evocative of possible crystal structure, but the interstices are packed in a chaotic manner.

In normal crystals we can assign three values (Miller indices) to label the observable reflections. In order to assign integer indices to the diffraction peaks of quasicrystals, however, at least 5 linearly independent vectors are necessary. (Dubois, 2002)

The necessary n vectors ($n = 5$ indices for polygonal quasicrystals and $n = 6$ indices for icosahedral quasicrystals) span an n -dim reciprocal space. Therefore there is also an n -dim real space in which a structure can be built that gives rise to a diffraction pattern showing the forbidden rotational symmetries. I.e. in non-random, higher dimensional constructs we can describe lower dimensional quasiperiodic arrangements as periodic ones. If we describe the structure in 3-dim space only, we would need thousands of atoms to represent a volume segment of the whole structure as well as all parameters that go with them (eg. thousands of positions).

A common example to illustrate the use of higher dimensions is a quasiperiodic sequence in 1-dim generated using a Fibonacci chain. The chain is a pattern of short and long segments that is governed by a higher dimensional space, V_2 , in which a 2-dim lattice is situated. Any

of the five 2-dim Bravais structures (oblique, rectangular, rhombic, hexagonal and square) can build up the lattice, with square being the simplest periodic structure to consider. Figure **B** shows the 2-dim lattice as a periodic repetition of dots. A set of axes define the orientation of two orthonormal **subspaces**, V_I and V_E . A subspace is simply a subset of a vector space. The 1-dim V_I (internal subspace) must be combined with V_E (external subspace) in order to complete V_2 .

A useful trick to remove the contribution from hundreds of lattice sites is to design a projection strip (yellow) to a finite width Δ . Figure 4.a) shows the **projection method**: all points in the strip are projected as a straight line onto the external space V_E , resulting in a quasiperiodic assortment of lengths designated either Short or Long in V_E . It is helpful to think of these lengths L and S respectfully as ‘tiles’ of the 1-dim space. Recognising that V_E is sloped with respect to the horizontal rows of the 2-dim lattice, α defines the tiles as:

$$a \cos(\alpha) = L, \quad a \sin(\alpha) = S$$

Equation 13

Consequently, $(\tan \alpha)^{-1}$ has to be irrational for an aperiodic sequence to be projected. Note that the closure condition of the strip is fulfilled provided that $\Delta = a(\cos(\alpha) + a \sin(\alpha))$.

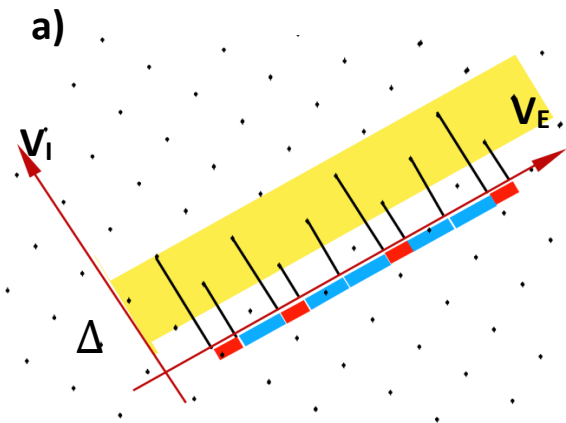


Figure 4.a) : The quasicrystalline projection of 2-dim lattice points from area defined by Δ onto 1-dim space: red lengths are short S , blue lengths are long L , forming a Fibonacci sequence.

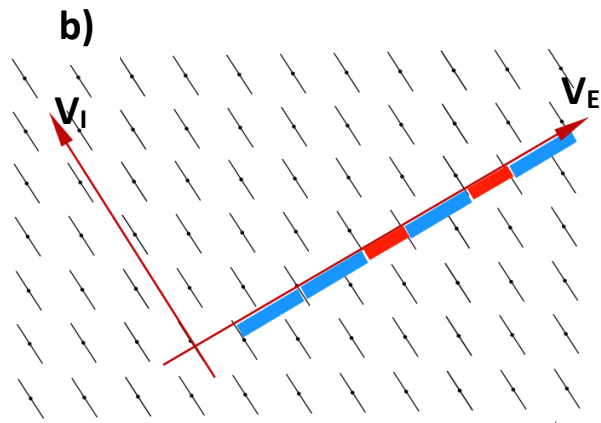


Figure 4.b) : The cut method also produces a quasiperiodic 1-dim structure.

The Fibonacci sequence has an irrational slope $(\tan \alpha)^{-1}$ that is equal to the golden mean, $\tau = 1.618\ 034\dots$. The golden mean has a recurring presence in the icosahedral symmetries, and is an important value in quasicrystalline structures.

Figure 4.b) shows the **cut method** in which a hyperplane (here a 1D-line) that is parallel to V_E cuts the higher-dimensional space. The occupation domains attached to each of the lattice points (here: bars) intersect with the hyperplane, producing the same quasiperiodic sequence as in the picture *a*). These occupation domains (the atomic basis as a 2-dim entity) extend parallel to the internal space V_I .

The cut or projection method can be generalised to an n -dim instance with $n = 5, 6, \dots$ etc. The contents of that n -dim unit cell consists of "hyperatoms" (occupation domains) which are analogous to the atoms in a normal unit cell. Therefore, quasicrystal structures in 3-dim can be describe with a finite set of parameters that exist in the higher dimensions. (Stadnik, 1999)

3. QUASICRYSTALS AND APPROXIMANTS

Quasicrystals can be categorised based on their structure. The two QC families that exist are **polygonal** and **icosahedral**. The first type has an axis of 8, 10 or 12-fold rotational symmetry of its crystal structure: they are periodic along this axis and quasiperiodic in planes normal to it. Icosahedral QCs on the other hand relates to a 5-fold symmetry and are aperiodic in all directions. Thermal stability also classifies QCs and their approximants into either **stable** or **metastable** phases. Stable QCs are the most ordered phases formed through slow-cooling / casting with subsequent annealing. (Tsai, 2009) However the process requires meticulous stoichiometry, one of the reasons that QCs are never found in nature (extraterrestrial Icosahedrite is an exception to this rule(Bindi, et al., 2011)). A metastable QC is made by melt-spinning or crystallisation of the amorphous phase. QCs can be made unstable if heated too extensively, and will revert back to a periodic polycrystalline phase upon melting.

The atomic structure of QCs is very difficult determine for two main reasons:

- The aperiodic lattice cannot be conventionally labelled using a unit cell and Miller indices. An example of a 2-dim quasicrystal lattice would be the well-known Penrose tiling; on the vertex of each tile lies a lattice point.
- The basis that decorates the lattice is not simple: instead of single atoms, clusters of atoms made up of concentric polyhedral shells are placed on the lattice points. The constituent elements that make up the QC can adopt different locations in the shells depending on the percentages of each element used during sample growth. In 3-dim the clusters can also orientate themselves at different angles to each other to reduce energy.

The simplest of **Penrose tilings** (see Figure 5) consists of only two shapes: rhombi related to each other by the golden ratio of their angles. The rules that match the squat rhombi to the thin ones determine that the tiling can continue indefinitely and never repeat itself, but also ensure that long-range order exists in the form of the underlying symmetry. Tilings such as these (others do exist through rules of deflation of the tiles into new tessellating shapes) are considered to be realistic models of growth for the lattice of quasicrystals: take for example Figure 6 which shows the aperiodic form of the *i*-Ag-In-Yb quasicrystal surface.(Sharma, et al., 2009) Notating these quasi-unit cells requires many more vectors than in conventional cells, as previously stated.

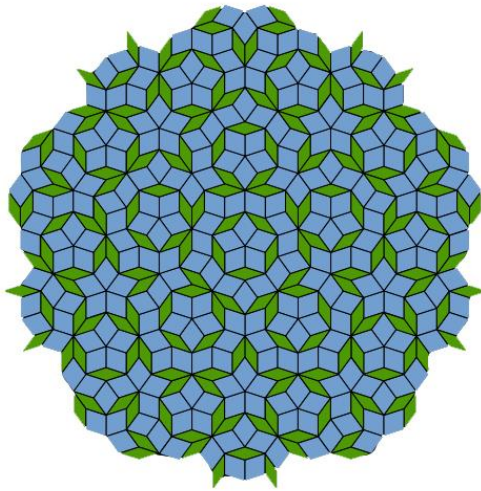


Figure 5: An example of the tessellating aperiodic P2 Penrose tiling. Matching rules prevent the system from becoming completely chaotic and result in an underlying forbidden symmetry – in this case decagonal.

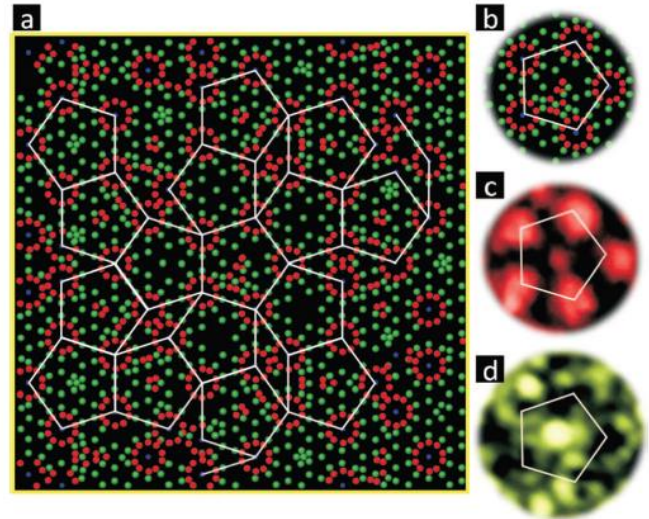


Figure 6.a) : The projected in plane structure for the fivefold surface of *i*-Ag-In-Yb over an area of 10x10nm. The central six pentagons are deflations of a larger pentagon. b) shows a single pentagonal unit. Also real STM measured height maps show the pentagonal unit obtain using different bias voltages: c) negative and d) positive.

3.1.1. CLUSTERS AND PLANES

Understanding the atomic structure presents yet another challenge. There are two different strategies for creating quasicrystalline model structures. One decorates the vertices of the quasi-unit cell tiles using information from closely related phases of the same atomic composition: i.e. for the *i*-Al-Cu(Zn)-Mg(Li) QC, squat and thin rhombohedra and a composite structural unit can (a rhombic dodecahedron) describe the 3-dim Penrose tiling lattice that obtains atomic motifs ‘borrowed’ from the structure of the Frank-Kesper phase Al(Zn)Mg. The Penrose tiling in this instance is generated from the projection method of a 6-dim lattice onto the 3-dim external space, and was experimentally confirmed with XRD data.(Stadnik, 1999)

The other strategy generates the atomic positions directly from 6-dim hyperspace. Positions and their occupation by different chemical species are determined by various properties of 3-dim atomic surfaces in perpendicular space. All quasicrystals have a ‘hard core’ which represents about 80% of the atomic position; these exist as 3-dim structures that can be described either in terms of local *i* **clusters** or alternatively in terms of dense atomic **planes** (projected from 6-dim hyperspace). The remaining atomic positions can be found via a comparison of XRD and approximant phase data.

3.1.2. PHASON FLIPS

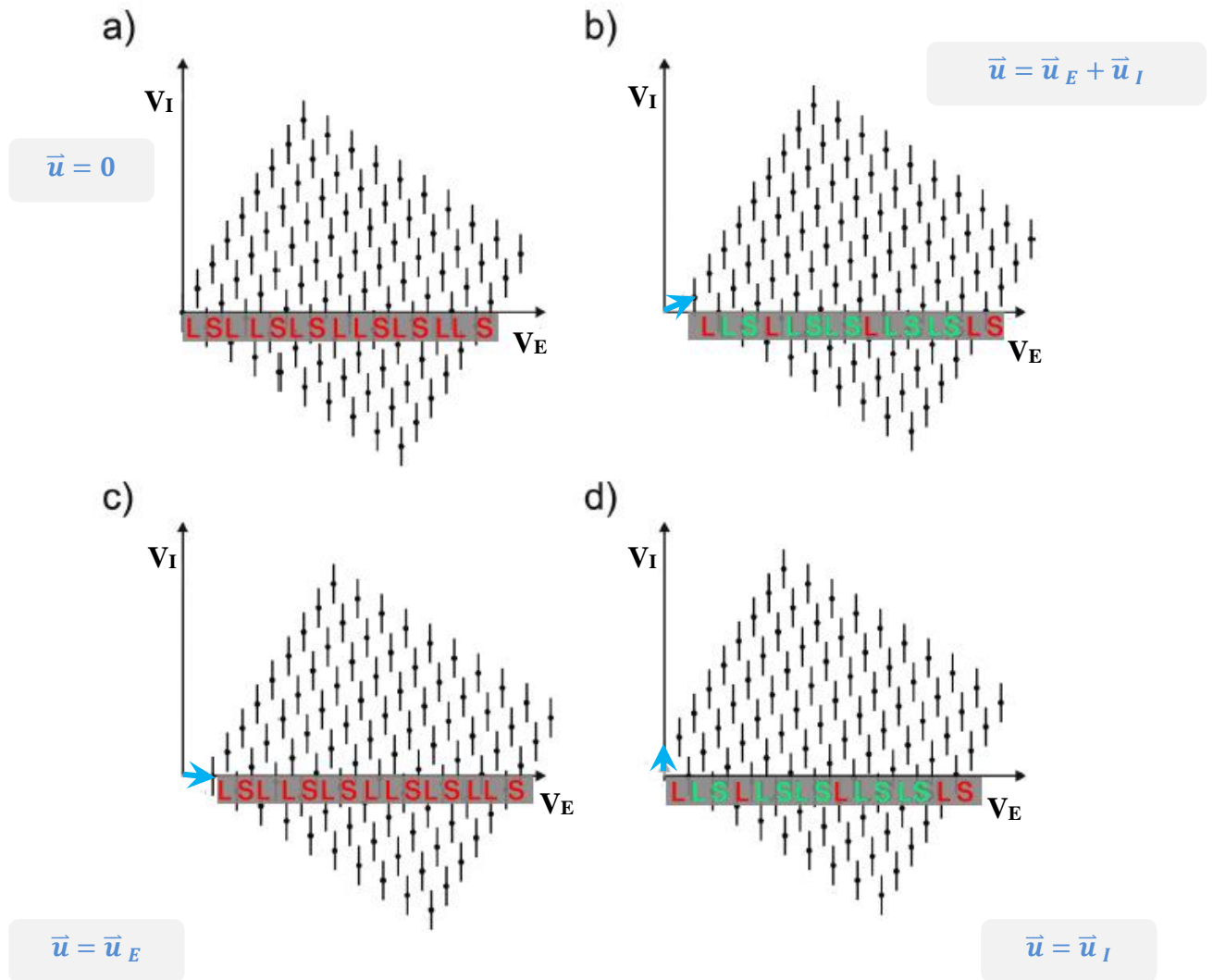


Figure 6: The cut method of producing quasiperiodic lattices can be seen here affected by displacement of the 2-dim architecture. A) shows the original 2-dim lattice producing a quasi-lattice, where the displacement vector is zero. B) shows the displacement vector (blue arrow) with components in external and internal space – the phason strain resulting from an excitation in internal space causes some of the lengths to swap around. C) and D) demonstrate how the flip only occurs when displacement in the internal space occurs. Phonons do not affect the structure of the external space lattice.

The additional dimensions of perpendicular space also have an impact on the elastic properties of quasicrystals: excitations of the lattice in external space (known as phonons) are complemented by an additional degree of freedom in internal space called phasons.

Consider Figure 6 where the Fibonacci sequence is represented by the cut method on external and internal axes. A displacement of the 2-dim lattice by a vector \vec{u} can be separated into displacements along internal and external space, i.e.,

$$\vec{u} = \vec{u}_E + \vec{u}_I$$

Equation 14

Periodic crystals have translational freedom in the external space, and a displacement in \vec{u}_E results only in a translation of the Fibonacci sequence as indicated in Figure 6.c). The related elastic excitations are conventional phonons. Quasicrystals on the other hand gain a non-zero \vec{u}_I displacement, representative of an additional degree of freedom in internal space, introducing a local rearrangement of atoms (for example LS \leftrightarrow SL). These jumps in atomic structure are also called **phason flips**.

We can find the elastic strain in conventional crystals using $\frac{d\vec{u}_E}{d\vec{r}_E}$: analogous to this is the corresponding phason strain leading to the phason flips $\frac{d\vec{u}_I}{d\vec{r}_E}$. Single-atom jumps were observed experimentally by transmission electron microscopy and their vibrational properties studied. (Ritsch & Nissen, 1996) Collective phason flips leading to the deformation of the tiling underlying the quasicrystalline structure have been also been observed. Phason flips are regarded as a key mechanism for structural phase transitions: this will be emphasised with respect to the approximant phase in the next section.

3.1.3. QUASICRYSTAL APPROXIMANTS

Approximant crystals are vital for our understanding of the effect of quasicrystallinity on physical and surface properties. They provide a study of a periodic structure made up of the same elements and structures as their QC counterparts. Quasicrystals and approximant crystals have a number of relationships to one another. One particularly illustrative relationship fits into the framework of our concept of a Fibonacci sequence: remember that the only thing distinguishing a periodic structure in 2-dim from a quasiperiodic one was the intersection of the occupation domains with the angled external 1-dim space vector.

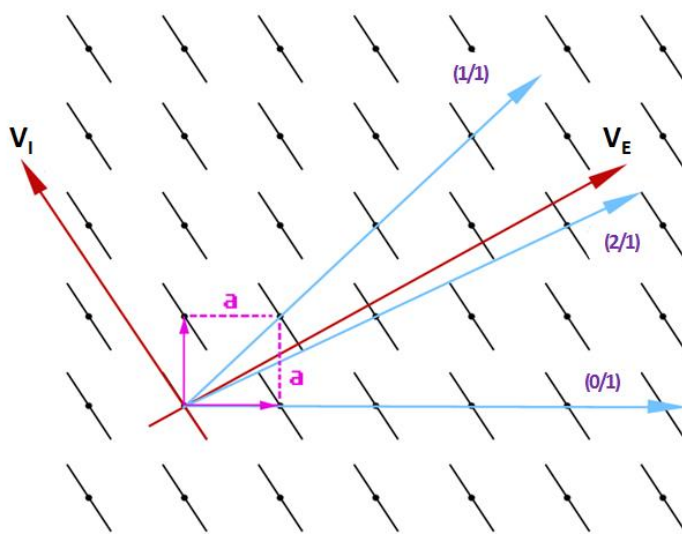


Figure 7: In the cut method the slope at which the external space axis intersects the 2-dim lattice can have irrational (red arrow) or rational (blue arrows) values. In the rational case, the sequence of slopes (0/1) (1/1) (2/1) ... etc represent periodic approximant lattices. The notation relates to the frequency that the line produced by a slope of (n/m) passes through the node of each atomic domain. Each successive member of the sequence gets closer and closer to representing the irrational slope $1/\tau$; hence the name 'approximant'.

Note that a slope equal to $1/\tau$ (as well as other irrational numbers) describes the condition when the external space vector passes through only one node of the square lattice – i.e. qualitatively a quasiperiodic structure. However if several nodes of the square lattice are intercepted by V_E then the 1-dim structure becomes periodic. In the previous section it was illustrated that a non-zero atomic displacement resulting from a phason strain leads to a change of atomic positions. A phason strain causing a rotation of the axes (equivalent to a shear strain within the crystal) can provide the necessary change in the slope.

The slope of the 0/1 line constructs the simplest repetitive pattern. 1/1 and 2/1 have a periodic repetition length of $a\sqrt{2}$ and $a\sqrt{3}$. The allowed rational slopes converge towards the $1/\tau$ value as they get larger (3/2... 5/3...), becoming a better approximation of the quasiperiodic lattice structure with each increasing order.

In summary, a ‘periodic approximant’ material can be thought of as follows: a deformation of the QC subspace intersecting the higher dimensional lattice, producing a periodic arrangement of points in 3-dim space.

3.1.4. TSAI CLUSTERS IN *i*-CD-YB

It is known that the same atomic clusters attach themselves to the higher dimensional lattice points are found in both QCs and in approximant from studies of the bulk using X-Ray diffraction of isostructural materials. (Sharma, et al., 2009) Detailed X-Ray structure determination of Cd-Yb QC 1/1 and 2/1 approximants found that the approximants were made up of large rhombic triacontahedral (RTH) units. These units presented well-defined chemical order, and were positioned in the case of the 1/1 approximant on a bcc lattice. (Gomez, 2003) The study of 1/1 Cd-Yb yielded the necessary information to tile the QC (3-dim Penrose tiling) and complete its structural model.

Soon after this accomplishment Takakura *et al* began work on other binary QCs that were of an isostructural nature to *i*-Cd-Yb. (Takakura, et al., 2007) The relationship between members of the *i*-Cd-Yb comes down to the number of valence electrons available per atom in the unit cell: in the case of the *i*-Cd-Yb quasicrystals this ratio $e/a = 2.0$; while in the approximant case the ratio is 2.09. This means that so long as elements similar in atomic weight and electronic structure replace Cd or Yb, and their proportion to each other in the alloy maintains this ratio, the new alloy will be almost perfectly isostructural. (Dubois, 2002) Figure 8 below explains why swapping Cd for Ag and In is viable.

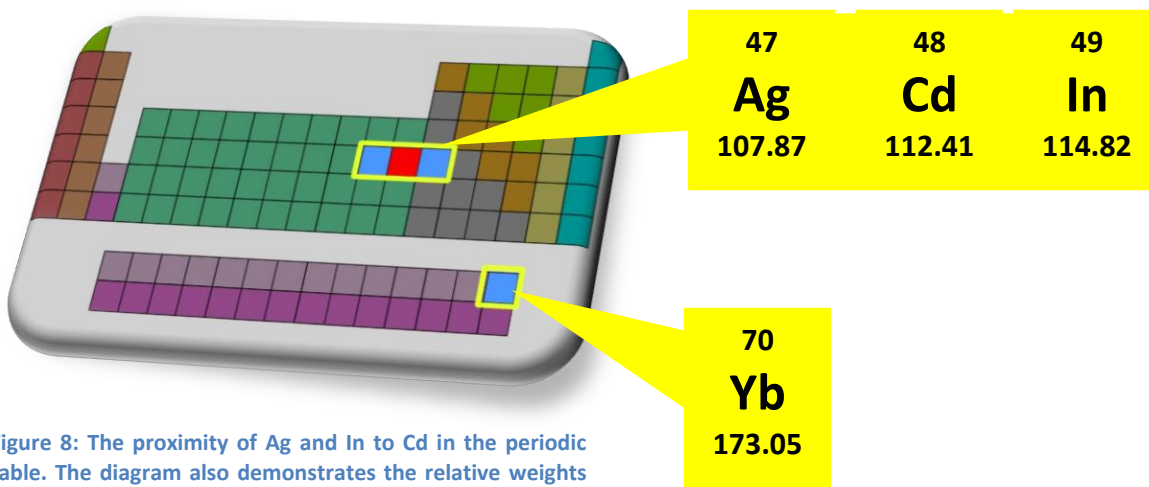


Figure 8: The proximity of Ag and In to Cd in the periodic table. The diagram also demonstrates the relative weights of the elements compared to Yb which is far heavier. This results in Yb forming much more stable bonds in the approximant structure than the other constituent elements.

The structure is made up of Tsai clusters. Each Tsai cluster is made of concentric shells as seen in Figure 9. The outer-most shell is the RTH unit, with successively smaller shells within. The decoration of these shells with each elements is shown (percentages indicating the most up-to-date theoretical placement of atoms (Shimoda & Gomez, 2011) for certain chemical compositions of the 1/1 approximant). Owing due rights to the scientist cooperating with the University of Liverpool from Tohoku / NIMS in this report, the model has been named the “Shimoda” model.

3.2.1. THE “SHIMODA” MODEL

Data from refinement of XRD data taken from an Ag-In-Yb approximant was stored in Crystallographic Information File (CIF) format and accessible through *IGOR Pro*. The data package that accompanies the CIF file is a specifically designed module used to explore the structure of the approximant. In this section the predictions of that model are obtained.

IGOR can be used as a visualisation tool and plots the position of atoms on the surface of a bulk-terminated approximant. Within the data module are a number of preset applications: one illustrates the density of atoms per plane as a function of the *z* coordinates in the crystal; another allows selection of a desired number of planes found in the model of the bulk structure and produces a 2-dim representation as if observing the sample top-down.

At any point the currently observed selection can be exported as a coordinate file (.xyz) which can be viewed in a number of other visualisation programs.

The immediately interesting features of the model are the symmetries involved.

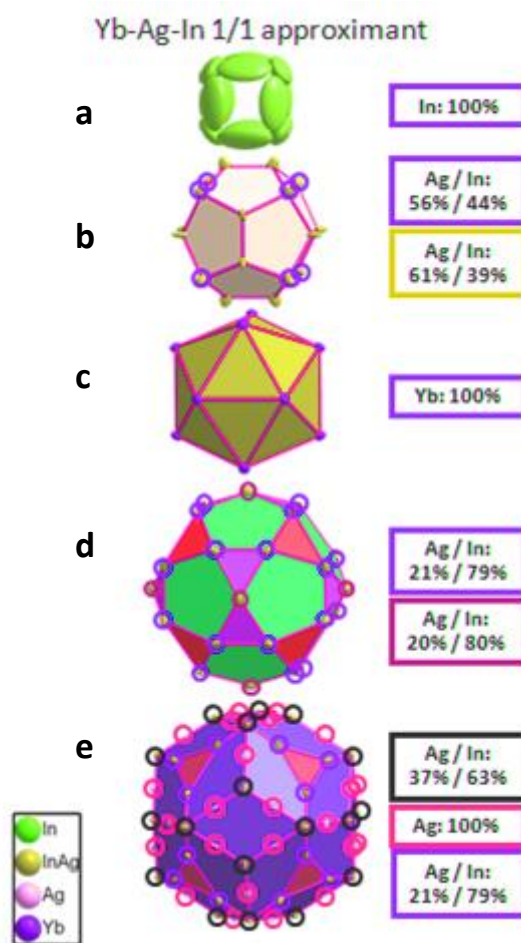
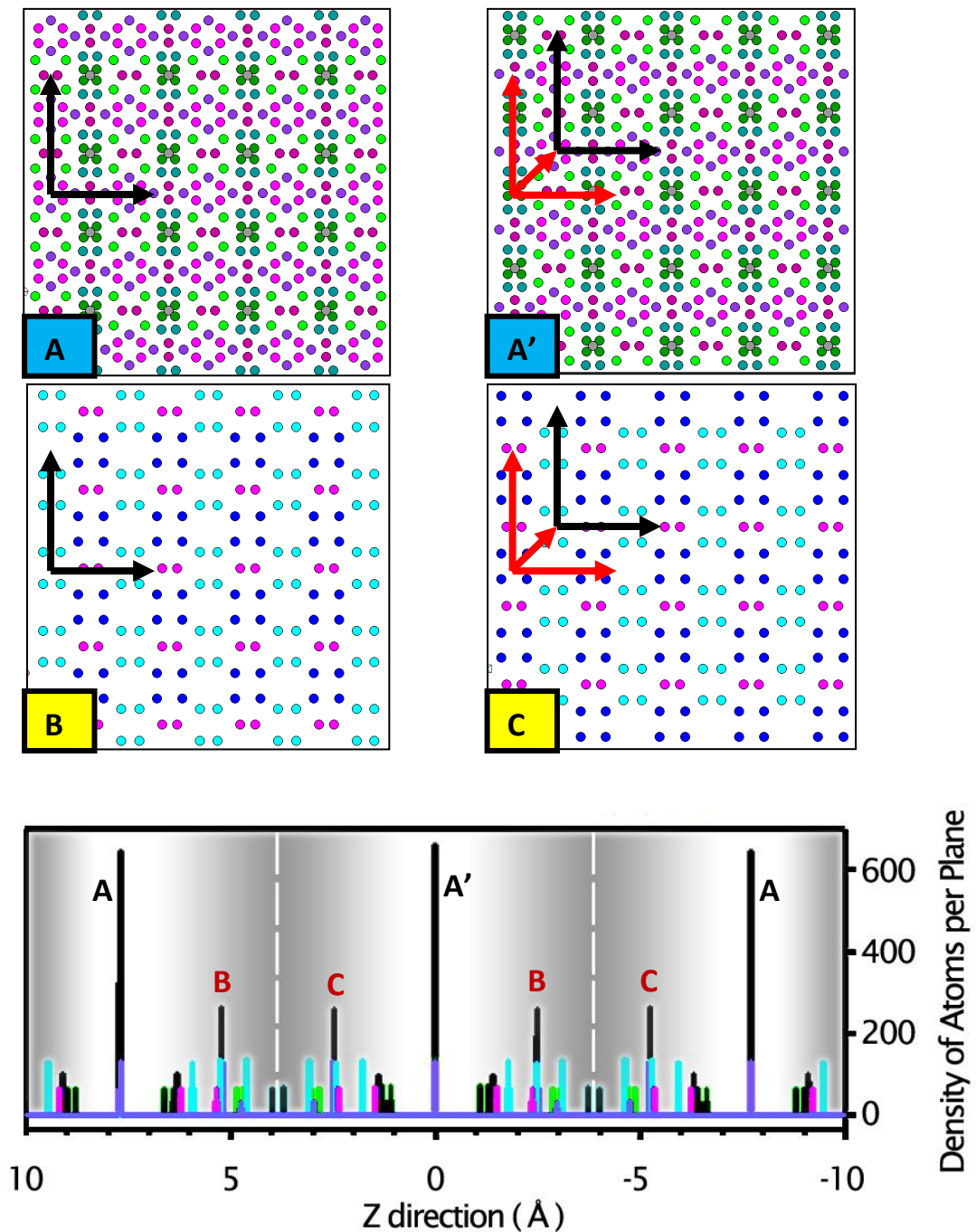


Figure 9: Atomic composition of Tsai clusters, made up out of a) a deformed tetrahedron; b) a dodecahedron; c) an icosahedron; d) an icosidodecahedron; and e) a RTH unit.

Figure 10 clearly shows a bcc lattice with cluster-like rings around core centres. The cluster centres (CC) are positioned on the lattice points of the bcc lattice, where the lattice constant a is calculated as 15.42\AA . The highest density planes parallel to the (100) surface intersect the cluster cores, whilst intermediate density planes arising from the overlap of clusters exist in between the CC planes. Due to the unit cell being body centre cubic, the sequence of high density planes shifts the cores along a translation of 45° when moving through the crystal in the z direction. (see Figure 10).

Figure 10: Top . Four images show the peaks of Fig.10 as (100) planes. All planes have a 2-fold basis symmetry attached to a 4-fold lattice. Planes A' and C are simply translations at 45° of the A and B planes, however the every plane is defined differently by the structure beneath the exposed plane.

Figure 11: Below. Density of atoms per plane is plotted against the Z axis over a distance of the bcc unit cell. The sequence of planes repeats throughout the crystal after mirroring around the A/A' planes.



The ‘in phase’ plane that has no translation is termed **A**, while the ‘out of phase’ plane is termed **A’**. The distance between these planes is $a / 2 = h_{AA'} = 7.71\text{\AA}$. Between the **A** planes are less populated planes: these mirror their structure about the **A/A’** density planes. In the diagram they are labelled **B** and **C**, and they show the same translational relationship as the **A/A’** planes. However the key distinction between **B** and **C** are the lesser planes ‘below’ them, which are different depending on where in the crystal the cut is made.

Table 1: the top area of the table shows all planes within half a unit cell of the Ag-In-Yb approximant, and highlights the predicted terraces/step heights most likely to occur in the topography of the Ag-In-Yb surface. Bottom values are the expected lattice constant and reciprocal lattice constant

Plane	Height in Z (Å)	Step Height	Step Height
A	7.71	-----	-----
	6.31	$h_{AB} = 2.47\text{\AA}$	$h_{AA'} = 7.77\text{\AA}$
	5.94		
B	5.24	-----	
	4.86	$h_{BC} = 2.77\text{\AA}$	
	4.66		
	4.62		
	3.99		
	3.73		
	3.10		
	3.06		
	2.86		
C	2.47	-----	
	1.78	$h_{CA'} = 2.47\text{\AA}$	
	1.40		
A’	0	-----	-----
Bcc structure lattice constant		$a = 15.42\text{\AA}$	
Reciprocal lattice constant		$a^* = 2\pi / a = 0.407 \text{\AA}^{-1}$	

3.2.2. PREDICTIONS FOR THE STRUCTURE OF AG-IN-YB

The table above shows the (100) planes inside a half of a unit cell that are predicted to contain atoms. The highest density planes are expected to appear in the greatest frequency when observing terraces of atoms on the surface of the Ag-In-Yb approximant; this is due to the high density planes possessing a greater thermal stability after crystal formation than the intermediate planes. During STM analysis we would expect to find the majority of step heights to be $h_{AA'} = 7.77\text{\AA}$.

The intermediate steps (h_i where $i = AB, BC, CA', AC, BA'$) are also expected to appear however with much lesser total coverage of the surface: manifesting in narrow terraces.

The separation of clusters is expected to be measured (using both LEED and STM) as $a = 15.42\text{\AA}$ in both x and y components. This is due to the 4-fold symmetry of the lattice upon which the clusters lie.

4. EXPERIMENT ONE: LEED

4.1 SURFACE PREPARATION

Oxidation studies on *i*-Ag-In-Yb yielded that no quasiperiodicity could be observed from a surface exposed to air, as the oxide is too thick (2 - 3nm layer) for surface analysis to be effective.(Nugent, et al., 2010) Isolating samples from air in vacuum conditions is therefore necessary to use techniques such as LEED and STM for surface structure analysis.

The cleaving method (sharp cutting of an alloy) of exposing quasicrystal crystal planes in UHV cannot prevent the atomic surfaces becoming roughened, making it an unsuitable method for examination of the approximant Ag-In-Yb surface. On the other hand, the use of ion bombardment (sputtering) and annealment in UHV on well-polished crystal samples yields atomically flat crystal planes(Sharma, et al., 2009). Appendix-1 provides a detailed adaptation of lab notes into a readable format for experimenters wanting to repeat experiments on Ag-In-Yb approximant samples. In summary of Appendix-1:

- The samples provided were both single-grain 1/1 approximants
- Both samples were polished using diamond paste (6 / 1 / 0.25 micron grain size) in order to make the (100) surface as reflective and flat as possible. STM and LEED require a flat mirror-like surface for optimum operation.
- A “sonic bath” was used to blast the surface with methanol molecules: the sonic vibrations from a water bath transfers energy to a beaker filled with methanol; sample is placed in the beaker and left for 15 mins every time a cycle of polishing has been completed so to reduce the chance of cross-contamination of polish grains.
- Spot welding fixed down the sample to a sample plate: this was made secure enough that the approximant crystal could not move or rotate in a tungsten wire cage when forced with tweezers.
- Argon ion sputtering (Filament current 30mA) and annealing of sample (400 - 430°C) clean the surface in UHV conditions: cycles on average of sputter: 40mins / anneal:

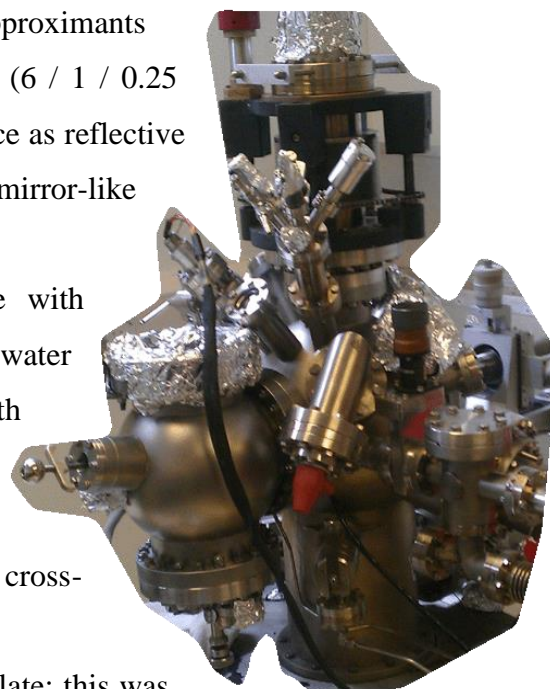


Figure 12: Photograph taken of Room Temperature STM chamber, University of Liverpool 2011.

2hrs respectively were performed under pressures of approximately 2×10^{-10} mbar. This pressure was 3×10^{-5} mbar during argon sputtering.

- Pressures were maintained through use of rotary pumps (10^{-3} mbar) turbomolecular pumping (10^{-10}) ion pumps (10^{-10}) and titanium sublimation pumping.

4.2.1. LOW ENERGY ELECTRON DIFFRACTION

In LEED, electrons incident on the surface of a sample are elastically backscattered (through the process of Bragg diffraction) and are analysed in an energy range of 20-1000 eV. Electrons in this range are excellent probes of surface structure because they possess de Broglie wavelengths of the same order of magnitude as the interatomic spacing between atoms / molecules at surfaces.

For a massless particle such as a photon diffraction is governed by the photon's wavelength substituted into the diffraction condition Eq. 7. For a particle with mass however, the de Broglie wavelength is calculated using the following equation $\lambda = h/\sqrt{2mE}$ where h m and E are Planck's constant, the mass and the kinetic energy of the particle respectively. For an electron this reduces nicely to:

$$\lambda(\text{\AA}) = \sqrt{\frac{150.6}{E(\text{eV})}}$$

Equation 15

This manifestation of wave/particle duality principle explains why electrons are able to undergo Bragg diffraction when they collide with a periodic structure. The de Broglie wavelength can be substituted into Eq.7 to give the angle at which the k-space vector intersects the nth rod on the Ewald sphere. In 2-dim this gives:

$$\theta_f = \sin^{-1} \left(\frac{1}{a} \cdot \sqrt{\frac{150.6}{E}} \right)$$

Equation 16

A reasonable assumption to make at this point is that the sum of the terms inside the brackets must not exceed unity or the arcsine becomes invalid. This puts a limit on the energy range for particular lattice constants in which LEED can directly probe the surface structure.

4.2.2. LEED APPARATUS

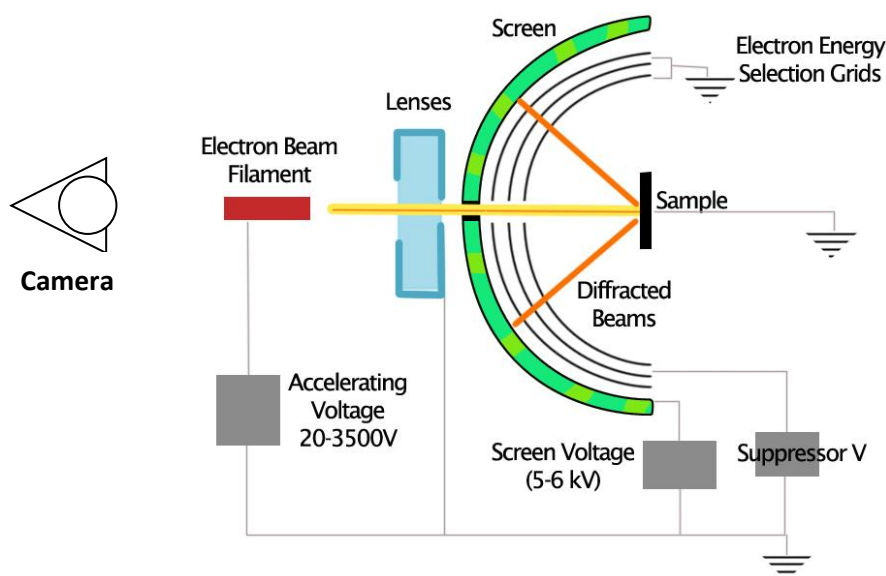


Figure 13: Diagram showing the apparatus required to observe Low Energy Electron Diffraction. The sample must be grounded to prevent charging.

The negatively charged electrons are produced monochromatically by a cathode filament at a negative potential. The energy can be varied by changing the filament current which heats the cathode. *Thoriated tungsten* or *lanthanum-hexaboride* filaments are used in Omicron LEED electron guns; both materials require careful monitoring due to sensitivity to misuse.

Exposure to reactive gases (for example H_2 , O_2 , H_2O) above 1×10^{-7} during operation can damage or poison filaments: this makes LEED exclusively operational in UHV. Electrodes in the gun act as electron lenses, focusing the beam to typical widths of around 0.1 to 0.5mm. The width of the beam must be comparable to the size of the surface in order to obtain strong diffraction peaks.

Modern LEED systems use a reverse view scheme consisting of an unobtrusive electron gun in front of a hemispherical transmission screen or position sensitive detector. The position detector (called a delay-line detector) has powerful resolution: it has charge-sensitive elements that focus electrons into $30 \mu m$ holes that sense the electrons presence and send a signal that is converted into X-Y coordinates. The expense of installing a delay-line detector means that a phosphor screen is more commonly used: providing a dark environment, one can observe the screen as it emits light locally from the intersection of the screen with diffracted beams of electrons. The diffraction pattern can be viewed and digitally recorded through a viewport in the chamber using a CCD (charge-coupled device) camera.

Only a small fraction of the monoenergetic electrons backscatter without losing any energy. The remaining electrons, due to strong interaction with matter, are found to be either completely absorbed by the upper atomic layers of the sample (related to the work function of the material) or are inelastically diffracted. Electrons can lose their energy through three main mechanisms:

- i) **Plasmon excitation:** quantized electron density oscillations of valence or conduction electrons in the sample. The quanta of energy involved in plasmon excitations are of the order of 10eV and depend on the nature of the substrate.
- ii) **Electron-hole pair formation:** an electron is promoted from a filled to an empty electron state when an energetic incident particle (electron/photon) interacts with the atoms / molecules in the sample. An energy loss range exists around 0-10eV.
- iii) **Phonon excitation:** atomic vibrations of the solid lattice are quantized and coupled. Exciting these quantized vibrations (known as phonons) takes little energy: a phonon typically is of the magnitude of 0.5-0.01eV.

The result of these mechanisms on the LEED electron beam is a spray of inelastic electrons that head towards the screen: recall that the angle of diffraction is related to the energy of the electrons and it becomes obvious that the wide range of potential will cause a relatively continuous background range of energies.

The LEED apparatus ensures that only electrons of kinetic energy of the primary beam E reach the phosphor screen. To strip away electrons of unwanted energy from reaching the screen, energy selection grids (collectively known as a field retarding analyser) are placed in the path of the backscattered electrons. Out of the three (or some cases four) grids used in the, the grid nearest the sample is connected to ground, facilitating a field free zone for the electrons to move through. The outer most grid, closest to the screen, protects the field free zone from the high voltages placed on the phosphor screen. The inner most grid / grids are at negative potentials and serve as cut-off filters to discourage low energy electrons. Finally, the phosphor screen itself maintains a positive potential to accelerate the electrons that made it through the filtering grids; if the surface has been well prepared, the majority of these electrons will have resulted from elastic scattering.

Table 2: Specifications for the Omicron SpectraLEED used for these experiments (OmicronNanoTechnology, 2003)

Screen Viewing Angle:	Spherical Radius:	Circular Diameter:	Electron Beam Current:	Screen Voltage:	Beam Energy:
102°	66mm	104mm	1.2A	4 - 5kV	30eV-160eV

4.2.3. LEED ANALYSIS OF AG-IN-YB

Through volunteering with the Surface Science department I was able to gain experience using the UHV system with a copper (111) crystal sample, and gained some of the skills necessary for my dissertation project. However, practising with Cu(111) was not a trivial pursuit. When analysing a sample through LEED, most of the structural information of the atoms is contained with the intensity of the diffracted Bragg peaks on the phosphor screen, which changes with respect to the energy of the electrons. Qualitatively we can use LEED to observe rotational symmetries and relative surface sizes of the unit cells. For example if a superstructure exists on top of the substrate, either some of the diffraction spots of the original pattern will increase in intensity, or completely new spots will appear).

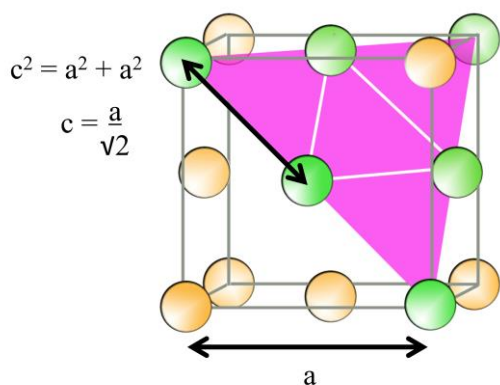


Figure 14.a: FCC lattice structure

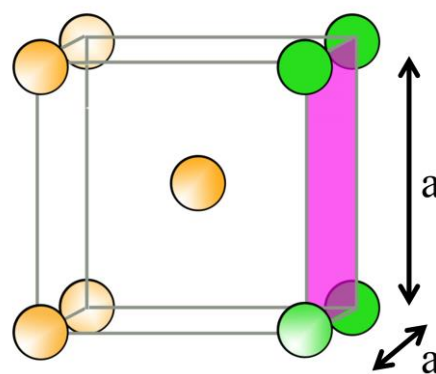


Figure 14.b: BCC lattice structure

The size of the unit cells of the superstructure can then be compared to that of the substrate through reciprocal space. This can be done because both the substrate and super structure have incident electrons of the same energy diffracting from them. They share the same projected reciprocal space unit vectors at that energy. It can be assumed then: when using the

same LEED optics and parameters, (e.g. *the distance from screen to sample*) that any two LEED patterns obtained at the same electron energy E share the same projected reciprocal space. Tremendously this allows for a quantitative appraisal of an unknown unit cell. A well known lattice constant can scale the reciprocal space seen on the screen, and thus a new pattern can have its lattice constants revealed.

A sample of Cu(111) was readily available for use. Copper has a face centred cubic (fcc) lattice with lattice constant $a = 3.615\text{\AA}$, and the (111) plane exposes a hexagonal arrangement of atoms (see Figure 14.a). Bragg diffraction works on the principle of constructive interference from surface atoms periodically spaced apart. The strongest diffraction comes from the planes of atoms separated by a distance close to the de Broglie wavelength of the incoming electrons, so the correct plane separation should be identified for use in *Eq. 16*. Figure 16 shows two possible diffraction directions along the (111) surface. (Sharma, 2011)

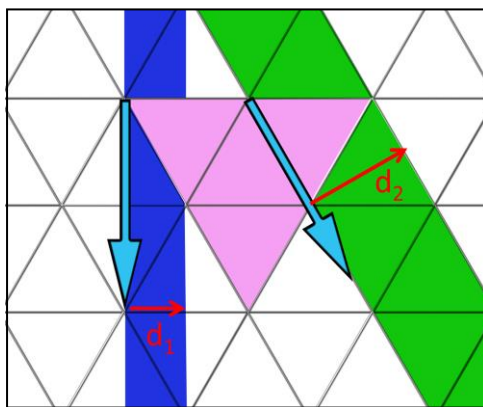


Figure 14.c: The selection of the correct diffraction distance is vital to obtain the correct diffraction angles.

Figure 14c indicates that the nearest neighbour atomic spacing in the (111) plane is $a/\sqrt{2} = 2.556$. From the geometry of the hexagonal Bravais lattice, made up out of equilateral triangles, values for d_1 and d_2 were calculated:

$$d_1 = \frac{a}{\sqrt{2}} \cdot \cos 60^\circ = 1.278 \text{ \AA}$$

$$d_2 = \frac{a}{\sqrt{2}} \cdot \sin 60^\circ = 2.213 \text{ \AA}$$

It would be natural to assume that the shortest distance d_1 would provide the strongest diffraction, however as stated previously, diffraction is governed by the matching of the wavelength (and thus the energy of the electron) to the planar spacing. The lowest energy value that obtained a suitable LEED image (see below) was at 65eV. Substitution into *Eq. 15* gives:

$$\lambda = \sqrt{\frac{150.6}{65}} = 1.522 \text{ \AA}$$

At this energy, d_2 will produce Bragg diffraction very close the maximum strength. However, it is likely that d_1 is too small to allow for diffraction. As described in the next section,

experimentally it was found that d_2 was the plane spacing that produced the Cu(111) LEED pattern.

It was not until some way into the project that a model for the Ag-In-Yb approximant structure was produced by Shimoda *et al.* The model gave a predicted lattice constant of $a = 15.42 \text{ \AA}$ for the body centred cubic structure, and the sample was cut along the (100) plane. The exposed (100) plane of a bcc lattice is square with lengths of side a .

It is non-trivial to estimate the plane separation that gives rise to a diffraction pattern. Recall the need to calibrate the LEED screen's coordinate system. To do this the LEED pattern for Cu(111) must be visible at an energy that accesses diffraction in the Ag-In-Yb system. If it is found that the calibration sample was unable to produce diffraction patterns at the necessary energies, another well-understood material could replace it: e.g. silicon (111) would be able to access different energies. Figure 15 shows calibration of the screen at 65eV, whereby the

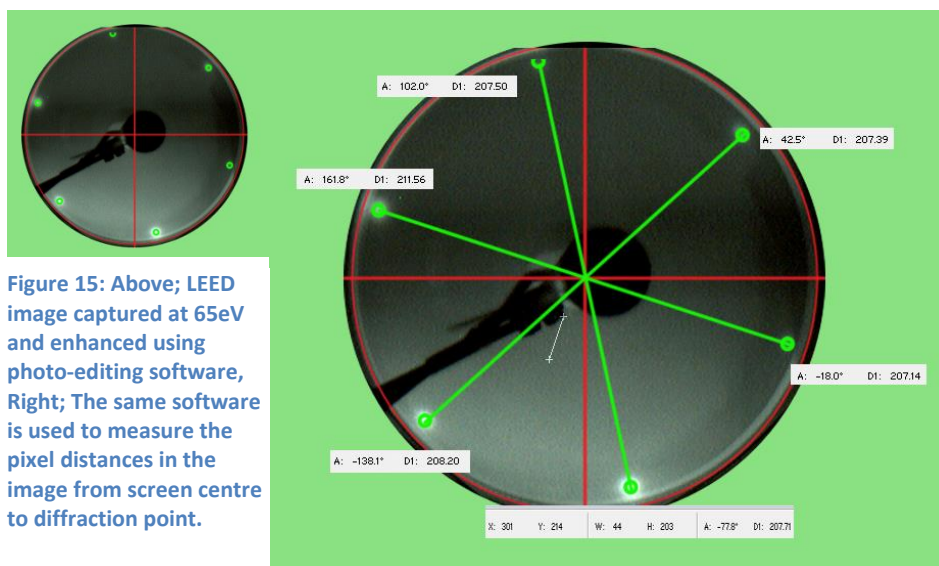


Figure 15: Above; LEED image captured at 65eV and enhanced using photo-editing software, Right; The same software is used to measure the pixel distances in the image from screen centre to diffraction point.

original LEED diffraction pattern is captured digitally, and the distance from the centre of the image to the diffraction spots R is measured in units of pixels: the pixel space is then made equivalent to that of the reciprocal lattice by taking the average distance R_A and equating it to the $\mathbf{a}^* = 2\pi / \mathbf{a}$. If the approximant pattern is able to reach this energy range then the scale (now in units of pixels) can be used to measure the reciprocal lattice vector of Ag-In-Yb.

There are cut-off energies from which discernible LEED patterns do not occur. For example in the case of Cu(111):

- For energies above 120eV a saturation effect is produced whereby the screen collected background diffracted electrons; electrons with more energy can travel further into the sample surface before being backscattered, causing them to diffract at a large range of angles.
- Below 65eV diffraction peaks simply did not exist: electrons with less energy are more likely to be involved in interactions with matter and thus tend not to be elastically scattered. They are prevented from reaching the screen by the retarding field analyser.

There are two more reasons why some E values will not provide a visible pattern.

- 1) In practise the LEED phosphor screen is not hemispherical, and instead spans a fraction of a sphere's surface so that the solid angle $\Omega = 2\pi(1 - \cos\theta_0)$. The Omicron LEED apparatus uses an angle $\theta_0 = 51^\circ$ so if low electrons are backscattered at an angle greater than 51° they will not be observed.
- 2) The size of the 2-dim Ewald sphere produced by the k-vector of the electrons is proportional to $E^{1/2}$ (see *Eq.16*) and for the reciprocal space lattice rods to intersect the sphere it must have a minimum radius. If $k_i = \frac{2\pi}{\lambda} = 2\pi\sqrt{\frac{E}{150.6}} < \frac{2\pi}{a}$ then Bragg diffraction will not occur and we will not see diffraction spots at that energy.

These observations can be made with knowledge of the lattice constant a . As was the case, most experimental work using LEED had already be completed before model for the approximant became available. Cu(111) was the only means of calibrating the screen, however the Cu(111) sample DID NOT reach the energy range required to calibrate the screen at an energy the approximant could produce clear diffraction spots. A compensation method is described in the next section)

4.2.4. LEED RESULTS AND DISCUSSION

The Cu(111) crystal sample produced a clear hexagonal pattern at $E = 65\text{eV}$. The R_A value calculated was 208 ± 4 pixels. The systematic error arose from the diffuse spread of the diffraction spots. The radius of the full screen in pixels was 228 pixels. The angle of diffraction can thus be found using the Omicron SpectraLEED specs in *Table 2*:

$$\text{percentage of screen radius} = \frac{208}{228} = 91.2\%$$

screen radius $r = 52\text{mm}$ optimum sample distance from screen $d = 66\text{mm}$

$$R_A = 208 \text{ pixels} = \frac{208}{228} \cdot r = 47.4\text{mm} \quad \text{Angle of diffraction } \theta_f = \sin^{-1}\left(\frac{R_A}{a}\right)$$

$$= 45.9^\circ$$

Checking that the Bragg diffraction theory agrees with this value gives:

$$a = d_2 = \frac{a}{\sqrt{2}} \cdot \sin 60^\circ = 2.213 \text{ \AA}$$

$$a^* = \frac{2\pi}{a} = 2.839 \text{ \AA}^{-1} \quad \frac{2\pi}{\lambda} = \sqrt{\frac{150.6}{E}} = \sqrt{\frac{150.6}{65}} = 4.128 \text{ \AA}^{-1}$$

$$\theta_f = \sin^{-1}\left(\frac{1}{a} \cdot \sqrt{\frac{150.6}{E}}\right) = \sin^{-1}\left(\frac{2.839}{4.128}\right) = 43.5^\circ$$

The angles match well, so we can assume that the LEED apparatus is functioning correctly and that our theory is correct.

Upon varying E between 28eV and 50eV Ag-In-Yb approximant sample produced its clearest square pattern at $E = 32.5\text{eV}$. The R_A value calculated was 44 pixels, and using the same technique as shown for the Cu(111) surface by measuring R_A in pixels, we find that the angle of diffraction $\theta_f = 8.7^\circ$. However, the beam energy was half that used for the calibration material diffraction pattern. Without another means of calibrating the LEED screen, a possible (albeit crude) solution was to predict where the spots from the copper would lie if they had been seen at energies of 32.5eV. Therefore the change in angle with respect to energy needs to be known. $\sin \theta_f$ is simply modified by a factor of $1/\sqrt{E}$ (see Eq.16) so if we half the energy we multiply $\sin \theta_f$ by a factor of $\sqrt{2}$.

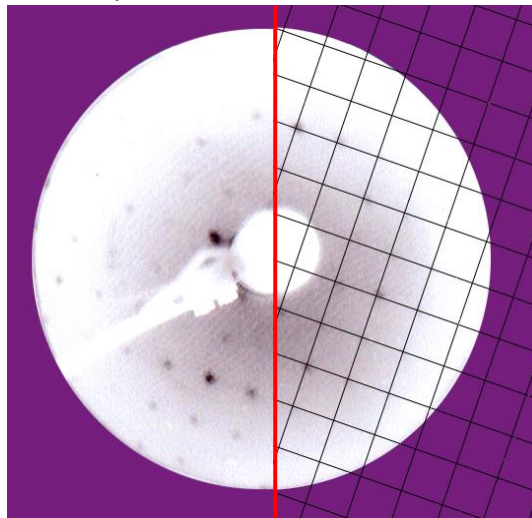


Figure 16: Photo capture of Ag-In-Yb LEED pattern modified using photo-editing software. Left: Inverted spots can be seen in black. Right: grid approximately matching the square reciprocal space lattice measures 44 x 44 pixels wide per grid square.

The experimental diffraction angle of copper ($\theta_f = 45.9^\circ$) at 65eV then becomes 76.6° at 32.5eV. This new angle corresponds to a new diffraction spot at a distance of $r \sin \theta_f$ away from the centre of the screen – equal to 60.6mm, or 265.7 pixels.

We reach the conclusion that 265.7 pixels are equivalent to the reciprocal space vector of the (111) Cu lattice and also that 44 pixels equals the reciprocal lattice vector for the approximant. Taking the ratio of the two and multiplying with the copper reciprocal lattice parameter $a^* = 2.839 \text{ \AA}^{-1}$ gives an estimate $a^*_{Approx} = 0.470 \text{ \AA}^{-1}$ $a_{Approx} = 13.364 \text{ \AA}$.

When compared to the modelled value of $a = 15.42 \text{ \AA}$ we see there is a 13% difference between a and a_{Approx} . The compensating method used tries to model an unrealistic scenario in which the Bragg diffraction laws are manipulated crudely: we could never observe low energy electrons diffracting from Cu(111) at such large angles because of the geometry of the apparatus and due to the reduced intensity of Bragg spots at lower energies. Large deviations from the true value are thus likely to occur, however the procedure demonstrates measurements of the same order of magnitude as the predicted values.

4.2.5. SUMMARY

- The LEED experiment was able to acquire diffraction patterns for both Cu(111) and 1/1 Ag-In-Yb (100) over various energies: the clearest patterns were obtained at 65eV for copper and 32.5eV for the approximant.
- Cu(111) could not access the low energy range that produced sharp diffraction peaks in the approximant system; instead a compensation method attempted to predict where Cu(111) diffraction spots would fall at 32.5eV (half the energy of its highest-quality diffraction pattern) in order to calibrate the LEED screen.
- a_{Approx} was measured to be 13.364 \AA with a 13% error.
- The compensation method provided a useful exercise in understanding the dependency of diffraction angle on energy.

5. EXPERIMENT TWO: STM

5.1. SCANNING TUNNELLING MICROSCOPY

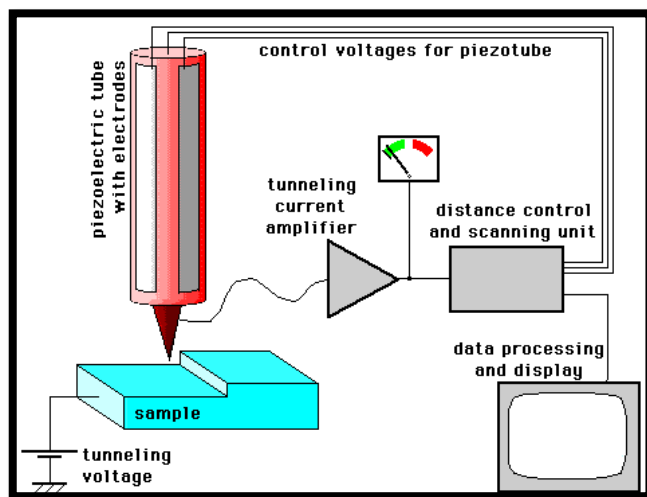


Figure 17: A well-known diagram showing the principle of piezoelectric control of a tip scanning over a surface. Detection of the tunnelling current feeds back into the distance control and scanning unit and maintains either a constant current or a constant height throughout the duration of the scan. The results are recorded in real time and displayed using digital imaging software.

LEED provides us with reciprocal space data generated by the long-range order present in a periodic crystal sample. However the LEED pattern is made up of constructive wavefunctions, and without measurements of the intensity of diffracted beams it ignores much of the nanoscale structural detail of the surface: it just doesn't paint a picture of the dramatically irregular topography of the surface. This was the job that the scanning tunnelling microscope (*STM*) was designed for,

and its creation and application in 1981 paved the way for a new era of science – the age of atomic resolution and manipulation as predicted by Richard Feynman in his famous 1959 speech “*There's Plenty Of Room At The Bottom*”.

A probing tip is attached to a set of three mutually perpendicular piezoelectric transducers, representing a Cartesian coordinate space (xyz). Piezoelectric transducers – or piezo for short – expand or contract when a potential difference is placed across them: upon applying a sawtooth voltage across the x piezo and a voltage ramp on the y piezo, the tip is able to scan across the xy plane. A sample is positioned beneath the tip and is brought to within a nanometre of the atoms on the sample surface. The tip (made of W or an alloy such as Pt-Ir) is atomically sharp so that a protruding atom is in closer proximity to the surface than all others. Typically for electrons to escape a solid they require energies of up to a few eV to overcome the work function of the material– in comparison the average thermal energy at room temperature can only supply energy of the order of tens of meV. Electrons in the tip (and sample) however can be encouraged to escape into vacuum through the phenomenon of electron tunnelling. Once brought near the surface the wave functions of the electrons in the tip overlap with those in the sample.

When a bias voltage is set across the tip and sample there is a shift in the density of states near the Fermi energy on either the tip or sample. For example a forward bias will provide a greater density of empty states in the sample as seen by electrons in the tip; for a negative bias it is vice versa. In both these cases electrons are encouraged to escape their bound states by an increase in tunnelling probability, and will flow to / from the sample. This can be measured as a tunnelling current. This makes STM a fantastic tool for surface studies, as it does not require a probing particle and only accesses surface electron orbits.

The tunnelling current depends on the lateral variation of electron density of the sample. These changes are mapped in images. Changes in current with respect to position can be measured, or the height, z , of the tip corresponding to a constant current can be measured. The larger the distance between the tip and the sample, the smaller the current is. This relationship is described by the equation $I(d) = Ce^{-d\kappa}$.



Figure 18: Omicron STM used in the RT-STM, University of Liverpool 2011

Table 3: Omicron Room Temperature STM Specifications

Maximum Scan Size:	Maximum Sample Size	Tunnelling Current:	Piezo Sensitivity XY:	Piezo Sensitivity Z:	Maximum Bake-out:
Typ. 2.3 x 2.3 μ m	11 x 11mm	20 pA – 50nA	9.5 nm/V	5 nm/V	180°C

5.2.1. AIMS AND HYPOTHESIS

The aims of STM image analysis of the backup data were to measure step heights and cluster separation using WSxM and Gwyddion software, produce a histogram of step heights h , and identify (100) planes in the bcc Ag-In-Yb quasicrystal approximant.

Studies of the occurrence of high density planes had not been published by other researchers at this time of writing, although data from 2009 had been presented by T. Yadav at the CMMP 11 convention showing evidence of terraces of intermediate planes **B** and **C**. The coverage of these intermediate density planes was small in comparison to the **A** and **A'** planes. This would imply that the intermediate planes would either occur less often or in

smaller sized terraces due to the lower stability of planes B/C. Hypothetically it was assumed that STM analysis would uncover a distribution of step heights representing a high frequency of $h_{AA'}$ step heights and a low frequency of h_{AB} $h_{BA'}$ $h_{CA'}$ h_{AC} h_{BC} providing that the images used in analysis contained many large terraces. The Shimoda model predicts the bcc lattice constant and the step height values to be:

$$a = 15.42 \text{ \AA} \quad h_{AA'} = a/2 = 7.71 \text{ \AA}$$

$$h_{AB} = h_{BA'} = h_{CA'} = h_{AC} = 2.47 \text{ \AA}$$

$$h_{BC} = 2.67 \text{ \AA}$$

Finding these step heights in the STM image data would indicate stable A/B/C/A' planes in an Ag-In-Yb approximant.

5.2.2. ORIGIN OF DATA

Originally it was expected that STM data could be collected and analysed during the start of the second semester of the year. Around this time a new sample of Ag-In-Yb had become available that promised to be of higher quality than the previous sample in terms of its thermal stability, size of surface, and surface level. It was found a lot less residual material was removed from the sample during extensive polishing, verifying an improvement in quality. The stable approximant sample was grown by Tohoku University using the slow-casting method. The previous sample was removed from the UHV chamber and put back into storage while the new crystal was prepared for analysis. This delay was furthered by other experiments on the RT-STM chamber obtaining priority. A new set of LEED images were taken in April, which were to be followed by a week of scrutinising the approximant via STM. With little assigned time left on the chamber, the compressed air system running through the Surface Science labs had used up its reserves: this was with great misfortune as the STM instrumentation requires isolation from large vibrations caused by mechanical pumps, and this was achieved through the use of a pneumatic valve. This rendered the STM practically unusable at ambient room temperatures – where thermal and mechanical fluctuations held greater influence over the quality of the images. Options to temporarily refit the chamber with an adaptation attachment for the compressed argon tank were disregarded as costly in both time and effort.

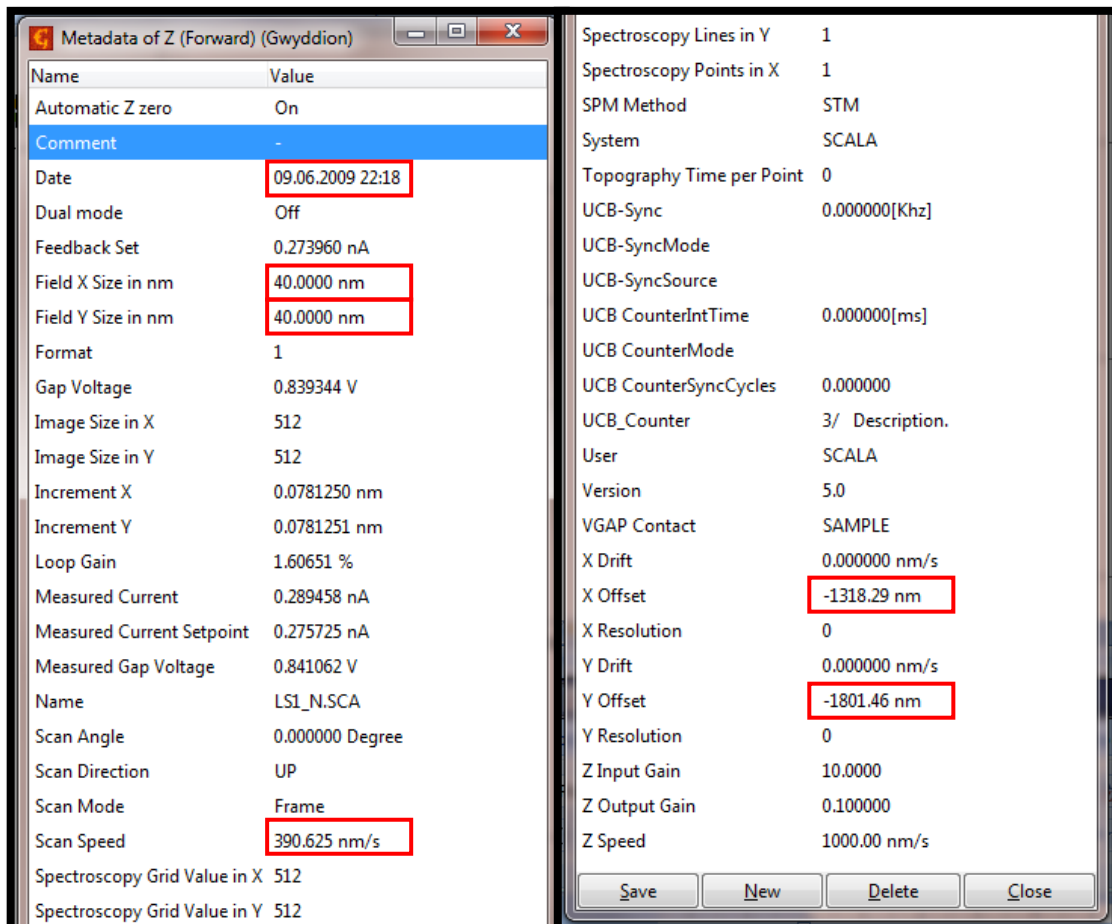
The project then fell back on unanalysed STM images recorded in 2011 provided by Sharma *et al.*

Background Information for 2011 Ag-In-Yb approximant data:

- Sample was cut in the (100) plane and prepared by polishing, then sputtering and annealing in a room temperature STM.
- Data was acquired by NIMS, Tokyo, Japan.
- The data set consisted of 115 .par files, a format of file containing z height maps of the forward and backward scan directions as well as the current map for every scan.
- Pixel resolution was 512x512px for all scan areas.
- Mapped scan areas ranged from 1x1 μ m to 20x20nm, with cluster resolution becoming visible at 100x100nm.

Lab notes with any specific experimental or laboratory conditions (room temperature, proximity to sources of vibration, STM malfunction or irregularities etc) did not accompany the data set; however the .par file format contains important information about the scanning process. Recorded parameters can be seen in Figure 21. The crucial information for this project included:

Figure 19: Information panel opened in Gwyddion. Highlighted in red boxes are the key parameters required place the the STM image data relative to other images



- Scanning amplitude of the x and y axes (scan area)/
- Scan speed in the horizontal direction.
- Probe tip's *xy* piezo offset from default central point; the centre point is where the tip positions itself after coarse movement using the piezo inchworm motor system.
- Time and date of data acquisition.

These four parameters were of exceptional importance in interpreting the data. The *axis amplitude / field size / scan area* provides a surface parallel scale that is used to identify the relative widths and lengths of key structural features. All SPM software packages build measurement tools that source their readout from the field size. The scan area is also useful in finding the *time constant*, in combination with the *horizontal scan speed*. Each scan is set to take a certain amount of time to complete. A complete set of data is usually taken using the same time constant, as this results in a resolution increase proportional to a decrease in axis amplitude: as the scan area gets smaller the tips speed decreases proportional to the time constant. Usually, initial scans are used to determine if there is anything worth investigating in the area selected, and data acquisition would take far too long to validate the use of large time constants. Knowing the time constant gives access to the *vertical scan speed*. The *xy piezo offset* and *timestamp* are crucial for knowing the order in which the height maps were taken and where they were taken relative to other images. Deficiency of this information means we cannot be sure the data is consistent with other images. Our need for consistency can be traced back to the aims of STM analysis of Ag-In-Yb. The STM exhibits a startling capability to zoom in on scan areas that are mere hundreds of angstroms wide. A great advantage of the Ag-In-Yb approximant is that clusters lie on the square lattice in the (100) plane with lattice constant $a = 1.54\text{nm}$: these features should be easily resolved at scan areas of $100 \times 100\text{nm}$. Atomic resolution allows us to go further and match atomic positions up against the model; it is the comparison of atomic model to terrace step height that quantitatively establishes which of the high density planes are revealed when a (100) cut is made through the crystal.

5.2.3. RELATED AND UNRELATED DATA

To arrive at atomic resolutions takes many attempts due to numerous factors: tip quality, tip crashes, surface quality, thermal drift etc. We must search across vast portions of the surface

landscape to find the perfect ‘atom-spotting’ site, and in doing so the tip is often retracted from the surface and coarsely. When approaching the surface once more it is almost impossible to find the same scan areas, especially on a sample more than x1000 larger than the maximum axis amplitude. All knowledge of the position of previous scan areas before tip retraction is lost.

Figure 22 shows a plot of the piezo offset for a several images that appear to be close together: without timestamp data these all are mapped to the same space simultaneously. We need to distinguish between related and unrelated data. The method following is designed as necessary to cope with the lack of lab notes to go with the data (and also no current STM software offers a way to map relate images to each other) but is not exclusively useful for STM images, and could be used for any SPM data that requires spatial mapping.

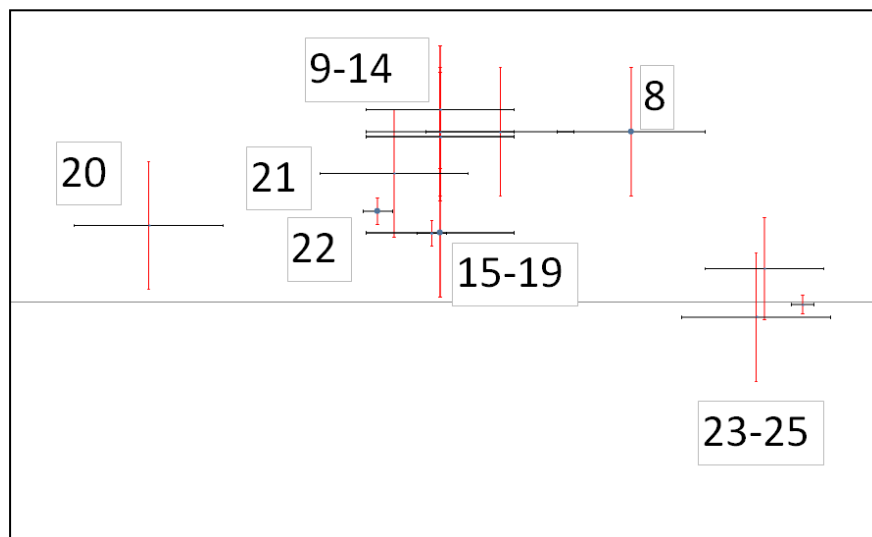


Figure 20: A plot of the piezo xy offset for each image. The images are represented by error bars of height and width equal to the image dimensions. The range of images 8-19 and 21-22 are all part of the same proximity group because they overlap and were taken consecutively; image 20 belongs to no proximity group; 23-25 belong to a different proximity group.

Method of proximity grouping to find related / unrelated data:

- Obtain parameters for each .par image file: *file name; xy offset values; timestamp; axis amplitude.*
- Arrange all .par image files and associated data into a chronological list.
- Plot each image as a point on a graph that has xy offset values as their coordinates.
- Label each point with its corresponding file name or number.
- Add to each data point error bars (horizontal and vertical) that simulate the size of the scan area.

- Record the identity of ‘proximity groups’ of data points that all fall within each other’s error bars. This indicates members of proximity groups may be images of the same area of the sample surface.
- Return to the list and then inspect the following:
 - A) how a group is composed of smaller and smaller images – i.e. once an experimenter has reached the highest resolution possible with the current area being scanned, he or she may choose to image a lower resolution image that is zoomed out above the high-res image... or may retract the tip in order to image another area elsewhere on the sample. It is thus unclear whether the piezo offsets are related to each other. Therefore it is best to assume from the chronological order of data acquisition that where scan area has increased from high-res to low-res (e.g. 40x40nm to 500x500nm) a new proximity group is formed. An exception would be if the offset remains exactly the same, suggesting that the tip has not been retracted.
 - B) whether any data points in each group were taken at times much greater than 90 mins* between each other – this suggests that although they share similar piezo offsets the tip has been retracted since then and they do not image the same area. The later images belong to a proximity group of their own.
- Result: raw data is sorted into proximity groups that the user can chronologically ‘travel’ through in order to zoom in on the sample.

*based on the time constant of the Ag-In-Yb scans, which would allow for many images to be taken within a period of 1.5hrs; this assumes that the experimenter would move onto a new portion of the sample after sufficient data acquisition.

The success of the proximity group categorisation was marred by the data set however.

Proximity groups in this data set were always composed of either:

- high quality terraces at scan sizes above 400x400nm but no cluster resolution and no underlying phase patterns picked up by FFT in images below 400x400nm.
- impossible to measure terrace images (blurry / streaked) but high resolution images of clusters below 100x100nm

An example is given below of the first case:

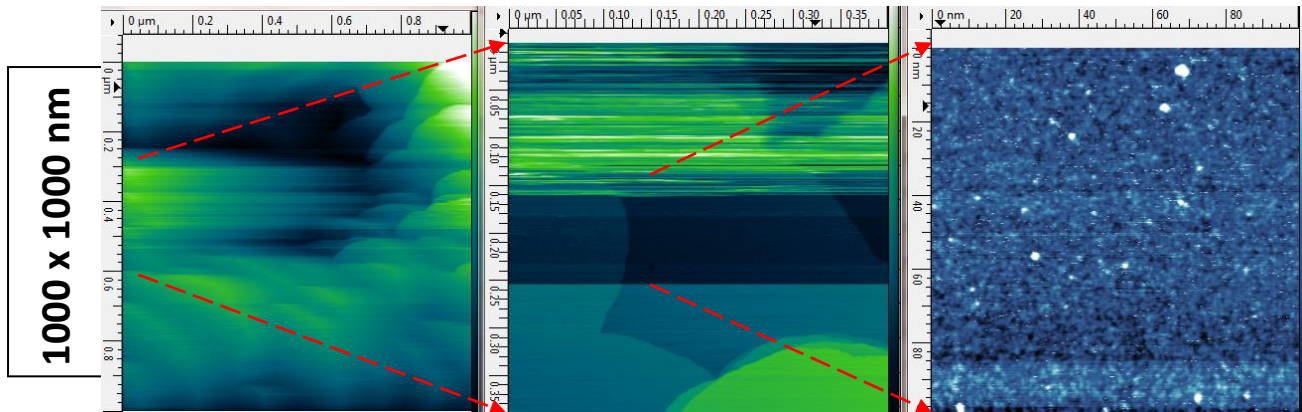


Figure 21: The above set of images is a proximity group as they share portions of the same scan area through the next image being a zoom of the last. Across the whole data set no proximity groups could identify step heights AND cluster separation, as shown here: the largest image is too distorted to use, however the 400x400nm image has large terraces and a step height available to measure. The final zoom into the terrace shows only noise and no underlying pattern (can be checked using FFT)

5.2.4. SPM SOFTWARE

Two software packages – WSxM and Gwyddion (*Gwyd*) were used to analyse the STM data in tandem with the Ag-In-Yb approximant model data stored in IGOR. WSxM and Gwyd are both freeware projects that can open a wide variety of SPM data files, including the widely used bitmap, .xyz and .par file formats. This section details the use of statistical filters such as FFT filtering, self correlation and plane subtraction in both programs. The filters and other techniques are able to highlight visual features of data that statistically would be impossible to comprehend, and as it will be made clear towards the end of this report, equal measures of intuition and experience make these tools invaluable to investigate structures as the nanoscale.



Figure 22: Plane filtered STM image of the 1/1 Ag-In-Yb (100) approximant surface

5. 3.1. UNUSABLE DATA

STM image data is heavily reliant on the tip and surface quality, as well as ambient effects such as thermal and mechanical vibrations. Below are a number of examples of different images taken that did not get selected for the data set, and why:



Figure 26: Example of tip not being able to reach into the depths of the surface – a streaking effect is produced as the tip tries to find electron orbits to image.

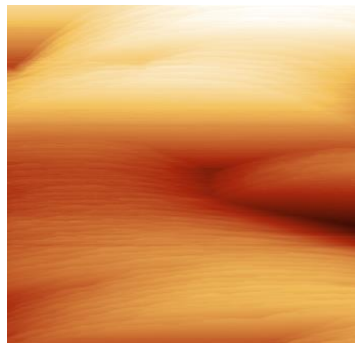


Figure 24: An unsuitable image. Too many narrow terraces suggest the scan area contains few stable terraces (which are the focus of this study).

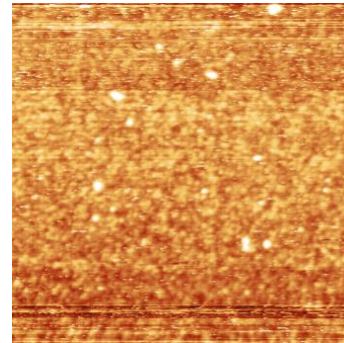


Figure 25: Noise can be generated from many different random sources – for small scan areas, if an FFT filter does not show the expected lattice symmetry (i.e. 2 or 4-fold) then the image is more likely just noise

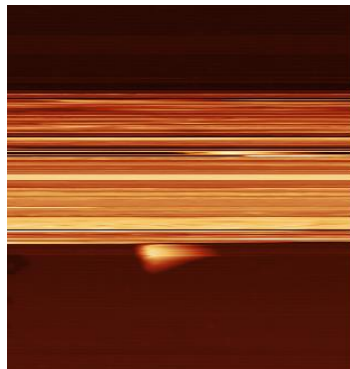


Figure 27: Tip crashing is often the result of a large island or irregularity on the surface, (i.e. the blob near the middle) and can cause damage to the tip as well as produce streaked images like this one. Applying a voltage pulse can clean the tip if it has picked up any residual matter from the surface.

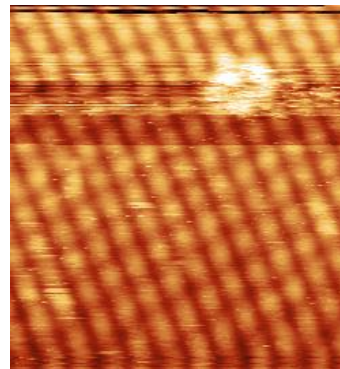


Figure 28: When a large offset is performed a DC voltage is applied to the piezos. The majority of the offset distance occurs quickly, but the remaining movement is slow. This slow portion of the travel is known as piezo creep. In images, creep causes distortion in the direction of the offset.

Thermal drift of the sample can also have the effect of distortion but tends to only occur in the slow scan direction and affects the whole image.

5.3.2. FILTERING STM IMAGES

Several processes in both *Gwyd* and *WSxM* can extract information about the atomic surface from STM images. Without these processes, the data remains qualitative and often very obscure to the untrained eye. The three main processes are plane averaging, FFT and self-correlation.

Plane Averaging

A collection of tools fall under this category of filtering, including: the correction of horizontal scars and streaks, subtraction of the average plane from the whole image, creating a local plane to subtract from the whole image, and row levelling. For the most part they are one-click or click-and drag operations on the height data. They should be used for the smoothing of noise or streaks, however work best when used on images with few major faults (this can be achieved through cropping the image). (See Figure 22) Careless use of these tools can however result in the loss of important information: for example, multiple local plane subtractions will change the height map so much it no longer represents the original image.

FFT

1-dim and 2-dim Fast Fourier Transforms are able to pick up one underlying patterns in STM images based on intensity and phase information. Sometimes images that look like they yield little information can be transformed when FFT is used as a filter to extract phase data. The FFT pattern represents a form of reciprocal space, similar to a LEED pattern, and the intense spots (as seen in Figure 29) are the contributions from all the components of the underlying pattern to the original image.

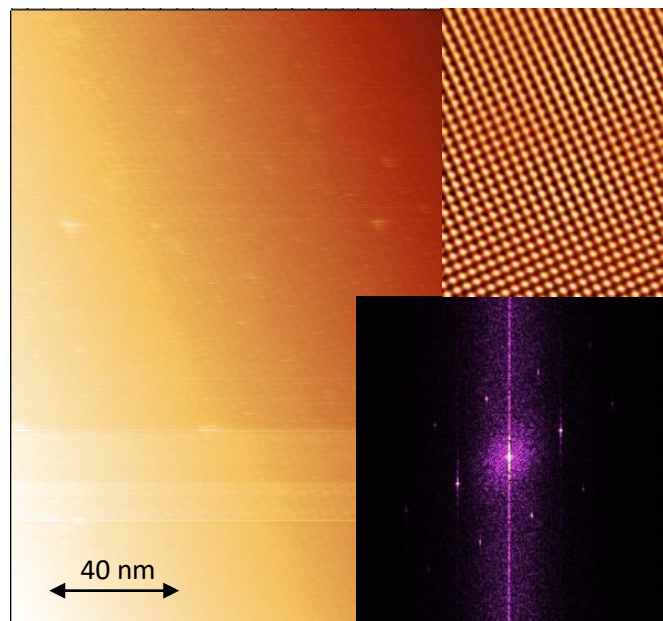


Figure 29: The large gradient image is the original STM data. The cross-hatched image is the underlying phase extracted by the Fast Fourier Transform in the bottom right corner. A square lattice can be observed in the FFT pattern and in the extracted pattern.

As with LEED diffraction, measurement of the vectors that make a lattice between the spots gives the reciprocal lattice vectors of the unit cell.

FFT filtering then extracts the pattern and creates a new image with only the phase information present (no influence from intensity). The new pattern is a good approximation of the position of atomic clusters, however the process to create the pattern is very selective and dependant of which intensity spots are selected to obtain phase information on and which are left out. Essentially any pattern can be extracted if the right phases are chosen, so knowledge of the unit cell geometry is essential.

Self Correlation

The self correlation technique is very similar to the FFT however does not depend on ‘phase’. Instead it looks at how different the original image will be when moved by a vector k . The more similar the shifted image is to the original, the greater the correlation. The correlation is given as an intensity which is plotted as a new image.

Thus repeating patterns can be enhanced by the self-correlation method without the need to manually filter in/out certain phases. This method doesn’t work well for images that possess lots of distortion however, which FFT is good at ‘seeing through’ to find the phase.

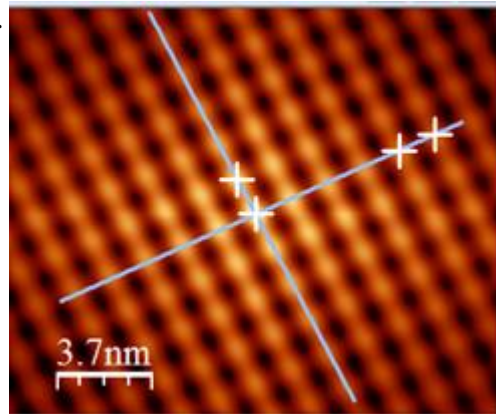


Figure 30: The correlation between shifted images produces the pattern shown above: it is subtly different from the FFT filter and does not require manual filtering. Each of the blobs is an atomic cluster.

5.3.3 TERRACE STEP HEIGHT AND UNIT CELL LATTICE VECTORS

The measurements for the terrace step height can be made using WSxM: by plotting a histogram of heights – once an image has been successfully filtered –terraces with large coverage of the surface will be identified by peaks in the height distribution. WSxM can slide markers along the histogram and measure the difference between the two heights: the difference between two immediately neighbouring peaks is equal to the step height between large terraces, and should equate to one of the step heights predicted by the Shimoda model.

To measure the unit cell lattice constants, Gwydd has a clever tool called an *averaging line profile*. The line profile can be drawn across a series of atomic clusters and create a 2-dim height map: the distance between peaks is the distance between the Tsai clusters.

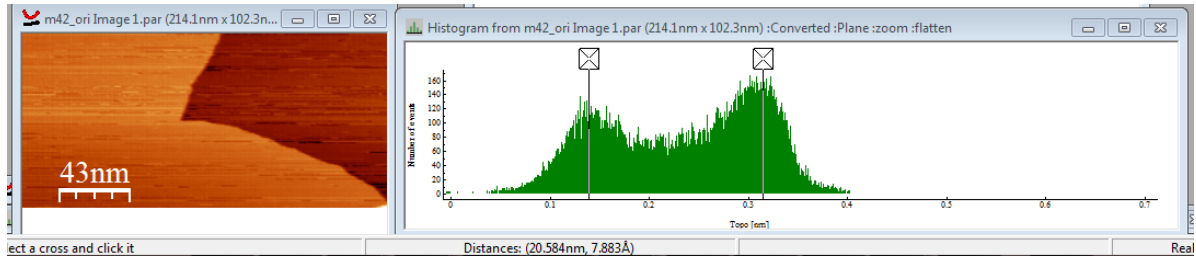
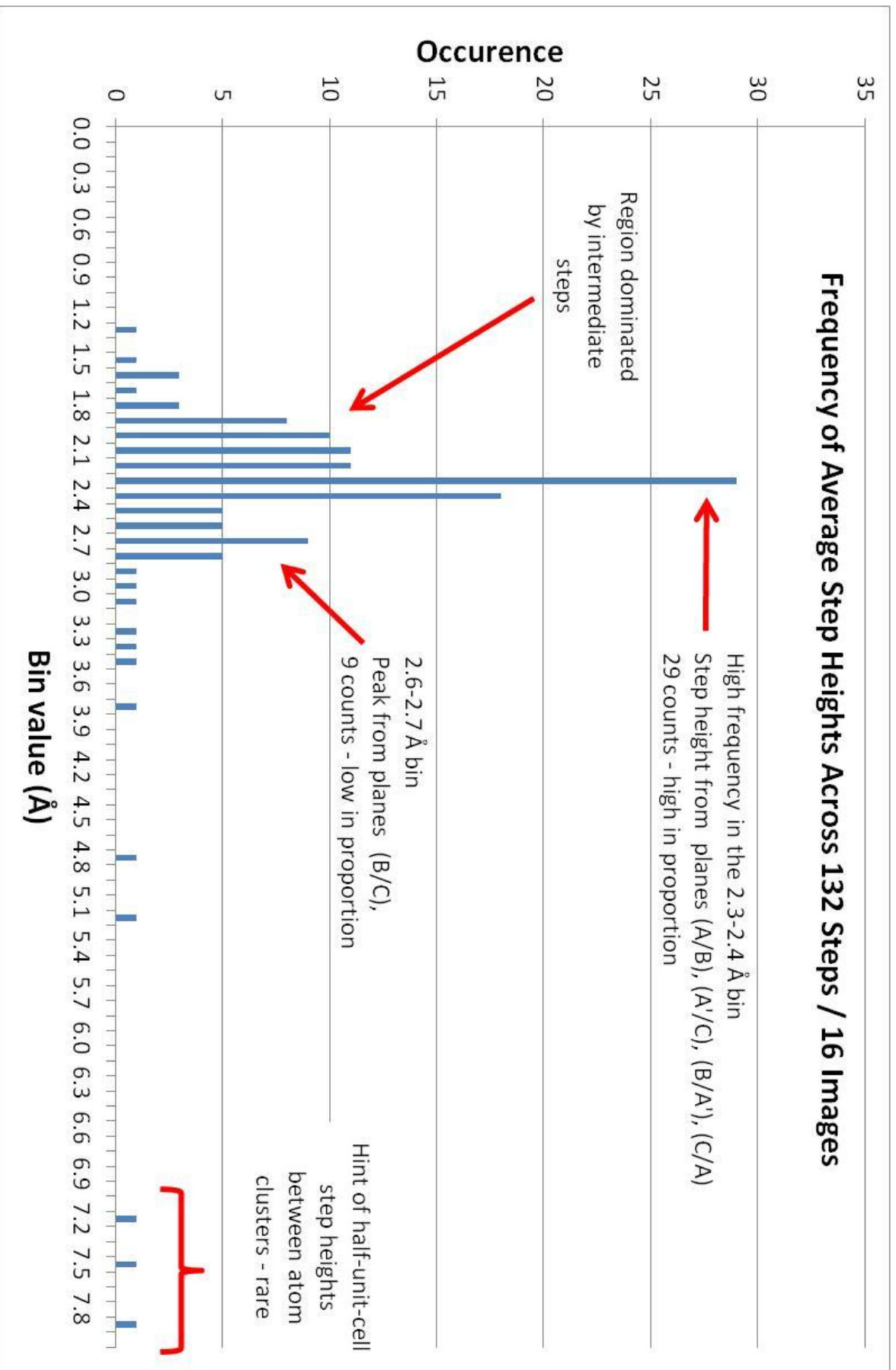


Figure 31: Example of the histogram method. The distance between the two planes (left) was measured as the distance between the peaks of the histogram (right). Here $h = 7.883\text{\AA}$.

Graph 1

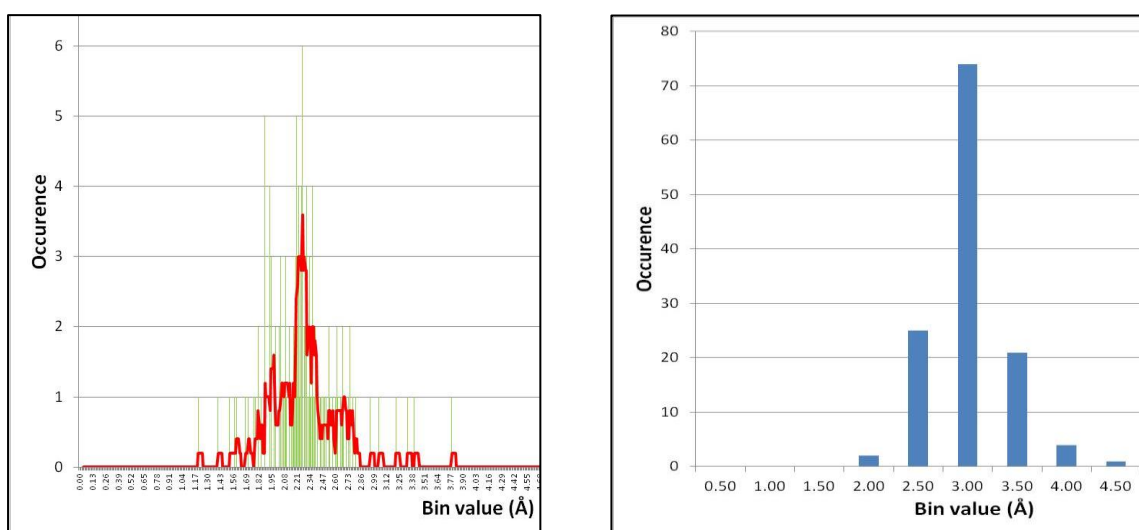
5.4. STEP HEIGHT



5.4.1. HISTOGRAM / RESULTS

A histogram of step height occurrence – *Graph 1*– showed some significant departures from the hypothesis. Three bin sizes were tested to gain an insight into the data: $S_1 = 0.5\text{\AA}$, $S_2 = 0.1\text{\AA}$, $S_3 = 0.01\text{\AA}$. S_2 is used in *Graph 1* and shows two Gaussian-like peaks. The S_1 histogram did not illustrate these peaks in enough detail, while the axis of the S_3 histogram was taxing to interpret: S_2 mediated between these two factors.

Graphs 2 & 3: Histogram data using bin sizes $S_1 = 0.5\text{\AA}$ and $S_3 = 0.01\text{\AA}$. See *Graph 1* for S_2 histogram

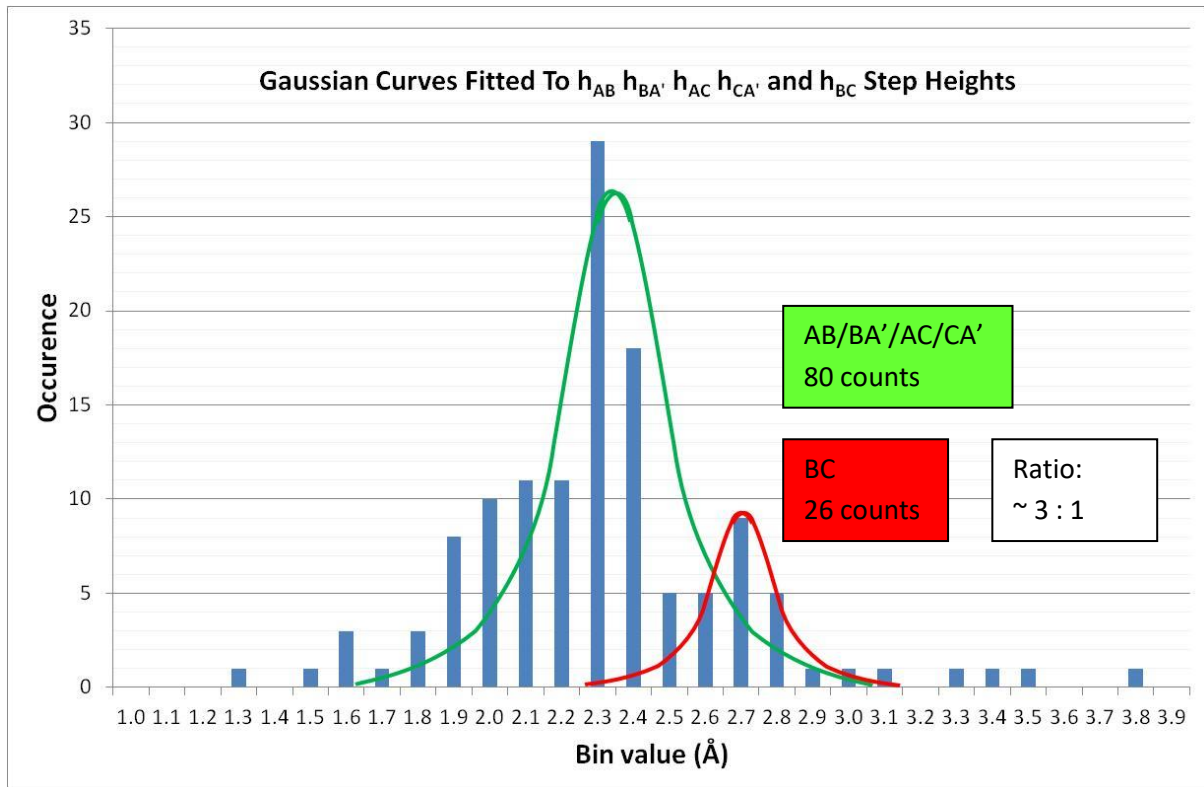


The hypothesis stated during the discussion of STM analysis predicted intermediate steps would occur in moderate frequency but that the expectation was to find high density planes A/A' forming the majority of large terraces. However *Graph 1* shows a clear abundance of the step heights corresponding to the intermediate steps for large terraces. The step height $h_{AA'}$ is rarely ever recorded, hinting at very stable structures existing in the cross over between clusters – i.e. B and C planes. The assumption that the high density planes are the most stable needs reviewing. Returning to the Shimoda model provided an explanation. Inside the unit cell there is a 2:1 ratio between the B/C planes and A/A' planes. Due to low data set population it was unlikely to measure this exact ratio and instead more likely to obtain an indication of this relationship.

The correct way to find ratios between peaks is to fit Gaussian curves to the histogram data. Statistically it is viable to collect up any counts found inside the bell-shaped curves representing the spread of step heights around a predicted value. *Graph 4* shows the procedure whereby normalised Gaussian curves have been aligned with the model step height

values and the scaled S_2 diagram is plotted beneath. A larger than expected ratio of the two curves was found: however we can assume that the data set is not representative of the true population, allowing for discrepancies in such statistical analysis.

Graph 4



What is also highlighted by the Gaussian curves is that the region to the left of the green curve, (see also *Graph 1*) appears to be uncharacteristically populated by values smaller than the AB/BA'/AC/CA' step height. Note as well that the bin with the highest counts is shifted away from the expected value $h = 2.47$ towards this region. If this region was produced by images of a single proximity group, it could imply that the group examined was anomalous. The region also had the possibility of belonging exclusively to very small terraces appearing between larger terraces. When investigating the raw data to ascertain whether this was the case, it was discovered that the smaller step heights were distributed regularly throughout most of the images, and so were not anomalous. However the associated terraces they were taken from almost always had very narrow surface coverage. The presence of this region can be removed from the ratio calculation so to reduce the size of the prescribed Gaussian curve and the number of counts under the curve.

5.4.2. DISCUSSION OF RIDGED TERRACES

To explain the high frequency of intermediate planes, we can call upon one possible solution: a modification of the Shimoda model that involves cutting ridged planes instead of flat slices through the clusters. (M. Krajčí & H.R. Sharma, 2012) (Publishing of paper pending: all the speculations below are made by the author of this report and not associated with the research carried out by Slovak Academy of Sciences) The refinement results in shifts of a group of atoms from their idealized positions and atomically flat layers of the ideal structure are modified.

The intermediate density planes B and C are at distances of 5.24 Å and 2.47 Å above the A' plane. Take the case where a cut is made through plane B and all material above this plane (coined here as the '**planar crust**') is removed. The binding effect of that crust material no longer impinges upon atoms on the surface of the B plane. Ag and In atoms in the B plane have low atomic weight compared to Yb, and will belong to shells in the Tsai clusters that have been removed with the planar crust. Recall that in the Tsai cluster bcc structure, the icosahedral shell of Yb atoms does not overlap into the crossover zone of the next cluster; while the outermost shells containing Ag and In will do so.

In theory the atoms in the overlap regions could either:

- ...be removed as part of the planar crust because of the lower energy bonds that the Yb. A ridged planar crust is removed and a ridged terrace is left behind possessing greater structural than the original B plane;
- ...undergo surface reconstruction to minimize the energy of the surface. This seems to be unlikely due to the bulk of literature documenting the preservation of the bulk structure at the surface of stable quasicrystals and their approximants. (Gomez, 2003) Surface reconstruction could however explain unaccountable surface features such as rectangular unit cells. (Franke & Berlin, 2003)

Cutting through a cluster at an intermediate plane will destabilise the cross-over structure of both clusters above and below the B plane. However it will only intersect the Yb shell of the cluster above the B plane and not below. In Figure 32 the proposed ridged plane is shown above A and A' planes. The Yb atoms rest very close to the surface of the ridges due to strength of its bonds. Figure 33.a) and b) highlight the icosahedral structure and show that

the planar crust removed from the top produces a stable surface that mostly uses the Yb bonds for structural integrity.

Figure 32: The proposed ridged model from the B/C planes. Instead of a flat plane being exposed, the removal of weakly bound atoms between the peaks of the blue line could produce a ridged surface.

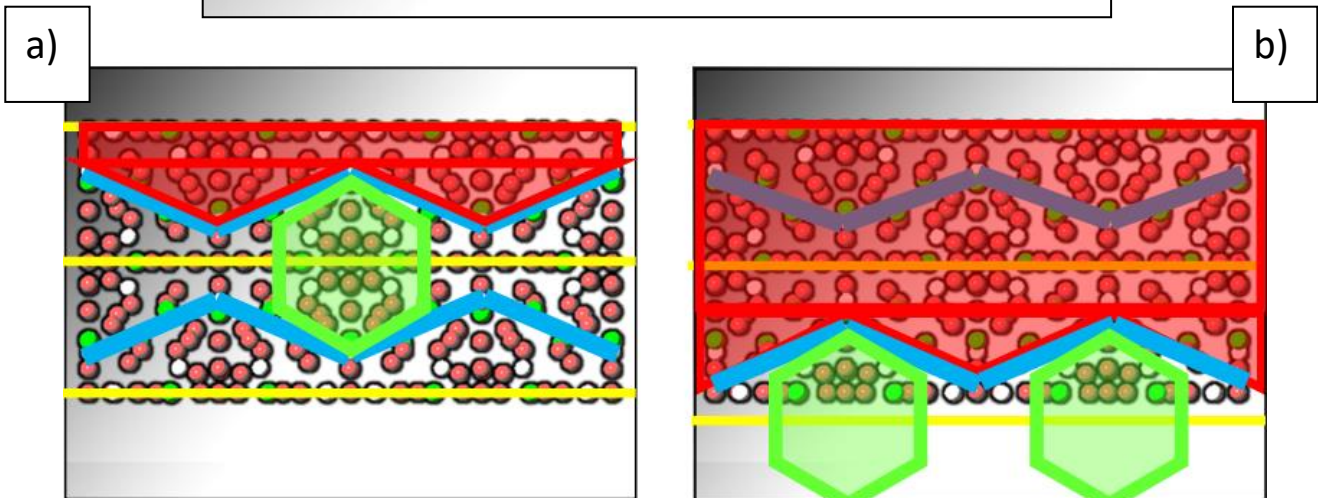
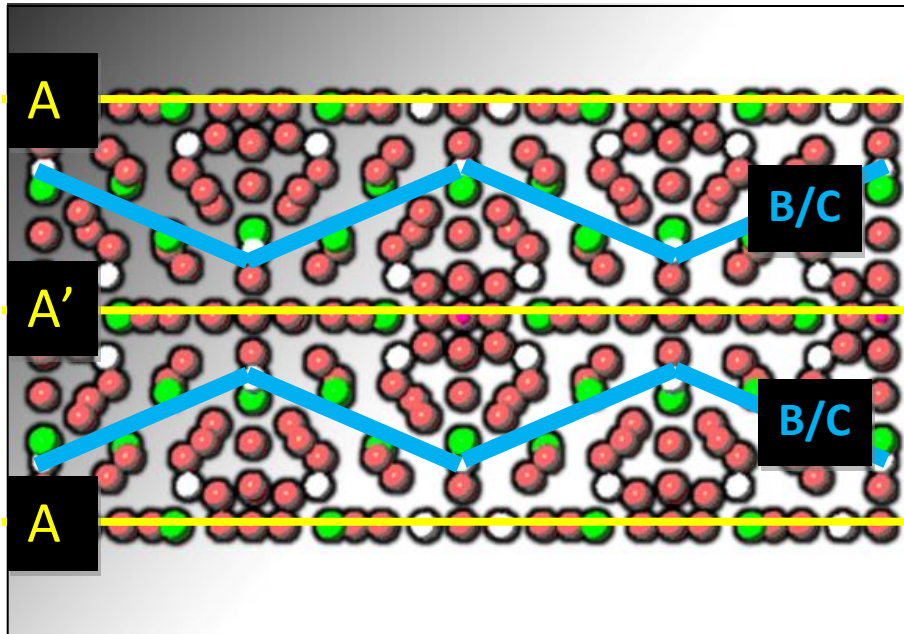


Figure 33.a) and b) showing the icosahedral shells in the Tsai clusters, providing strongly bound structures within the ridged surface. The red zone indicates the removal of the planar crust, leaving behind the ridged surface.

5.4.3. ERROR ANALYSIS

The mean value of all step heights was calculated as $h_{avg} = 2.429 \text{ \AA}$ ($\sigma^2 = 0.849$). The variance accounts for the smaller step height values and the intermediate terrace signature peaks.

The sample data population is too small for quantitative conclusions to be made: the nature of scanning tunnelling microscopy in this project is, like LEED, mainly a qualitative analytical process. This makes an assessment of the ‘error’ on values somewhat futile. Values of the average step height per step collected from 16 images were arranged into a data set that consists of no measurable error. Statistical error is reduced by using the height map histogram sliders to intersect the centre of Gaussian-like peaks in the terrace heights: this software feature removes much of the hassle encountered in trying to fit profile lines across step edges. (see section). Systematic errors on the step height are related to the quality of each individual image mapped by the STM – this is affected by piezo creep, thermal drift and STM system calibration. Other issues such as tip crashing or a dirty tip will usually leave an image unsuitable for analysis, rather than producing error. Now we left to quantify the effects of creep, drift and calibration, and it becomes extremely difficult to account for systematic error. In the z axis the piezo system cannot ‘creep’ – this is an effect on the horizontal plane piezo offsets only. Drift is mainly considered in the xy plane and this does not affect the step height measurement by a great degree. Any z drift is usually removed during filtering through average plane subtraction. Finally, the calibration of the STM itself is unknown in the absence of lab notes. The action taken to analyse results was to instead to calculate the variance of results from expected values found in the Shimoda model through standard deviation.

5.4.4. SUMMARY

- The data population was too small to make any asserted claims of accurate step height measurement. In light of this, peaks in the step height histogram were found to concur with the Shimoda model intermediate structure.
- Intermediate step heights belonging to planes A/B, B/A’, A/C, C/A’ and BC were observed in much greater occurrence than the expected planes AA’ that separated cluster cores.
- *Expected peaks from intermediate planes:*

$$h_{AB} = h_{BA'} = h_{AC} = h_{CA'} = 2.47\text{\AA}, \quad h_{BC} = 2.77\text{\AA}$$

- Gaussian curves were fitted to the histogram to establish ratio between step heights.
- The ratio of step heights ($h_{AB} h_{BA'} h_{AC} h_{CA'}$) to (h_{BC}) was found to be approximately 3:1 which was larger than predicted, however a group of small step heights belonging

to narrow-coverage terraces could have weighted the data set in favour of a larger ratio: future data sets should exclude narrow-coverage terraces.

- The stability of intermediate B and C planes may be a result of a ridging effect in the surface upon the removal of planar crusts.
- STM image analysis techniques removed much of the statistical errors encountered at the nanoscale level thanks to plane averaging and histogram height selection.

5.5. CLUSTER SPACING

The model predicts that cluster cores are periodically separated by a distance of 15.42Å in the (100) plane upon a square lattice. From analysis of the terrace coverage in the previous chapter it is apparent that different terraces are not going to exhibit the same atomic structure as each other: a quick check of the Shimoda model reveals different atomic arrangements for planes A' B C and A.

5.5.1. MEASURING X AND Y LATTICE COMPONENTS:

It was originally planned to choose images by criteria that gave preference to the highest resolution images with evidence of steps between terraces alongside cluster or atomic structure. However out of the entire collection of images none met these criteria – only one image reached cluster resolution with step height information. The next preferable type of image would also have atomic resolution and would be located inside proximity groups so that the atomic decoration could be compared against terraces: thus planes could be identified. Again, this criterion went unfulfilled as very few images could achieve atomic resolution. Those that did are discussed in detail. Finally, images that obtained cluster resolution and were locatable within a variety of proximity groups were the last desirable form of data that could measure the lattice constant a . Twelve images made up this last group and were all filtered using FFT and self-correlation. Measurements of the horizontal lattice components a_x and a_y were made using both averaged and single measurement line profiles. Measurement of the reciprocal space vectors in FFT patterns was also taken from several STM images (although due to a departure from the Shimoda model, only line profile data is presented to highlight the repeatability of the found result).

4a)

Image number	X 1	Y 1	X 2	Y 2	X 3	Y 3	X 4	Y 4
52	1.518	1.49	1.637	1.347	1.597	1.406	1.478	1.394
52	1.496	1.419	1.564	1.303	1.507	1.28	1.567	1.396
55	1.64	1.375	1.443	1.387	1.561	1.281	1.482	1.328
55	1.573	1.274	1.592	1.38	1.514	1.309	1.632	1.321
60	1.553	1.306	1.671	1.353	1.474	1.341	1.592	1.282
60	1.526	1.341	1.506	1.322	1.605	1.303	1.605	1.341
60	1.455	1.367	1.552	1.386	1.63	1.31	1.455	1.462
67	1.578	1.348	1.512	1.367	1.534	1.291	1.489	1.386
67	1.563	1.357	1.518	1.28	1.674	1.338	1.518	1.319
67	1.594	1.331	1.616	1.312	1.483	1.369	1.616	1.35
71	1.418	1.383	1.616	1.305	1.573	1.344	1.506	1.422
...

Table 4a) and 4b): examples of data set for unit cell vector data collection

...	Average X	Average Y
52	1.5524	1.36375
52	1.5637	1.341
55	1.5376	1.346125
55	1.542	1.338875
60	1.5523	1.3475
60	1.5348	1.338625
60	1.542	1.366625
67	1.5294	1.345625
67	1.5581	1.342625
67	1.5616	1.34525
71	1.5339	1.35625
...

4b) An extract from a complete data table highlighting the rectangular lattice components previously unseen in the model

5.5.2. RESULTS

Despite the model's predictions of square lattice features, y lattice components of many of the terraces imaged were less than $a = 15.42\text{\AA}$. An average factor of 0.882 scaled the component a_x to a_y and this behaviour was observed across ten of the twelve images selected for analysis. This revelation required a new appraisal of the Shimoda model. Here it is identified that a rectangle in the A/A' plane with sides a_x , a_y approximately 13.23\AA and 15.42\AA exist in between cluster cores. (see Figure 34) The ratio between these two lengths matched the average scale factor measured from the STM data. Similar rectangles can be found in the B and C planes possessing a length ratio of 0.832.

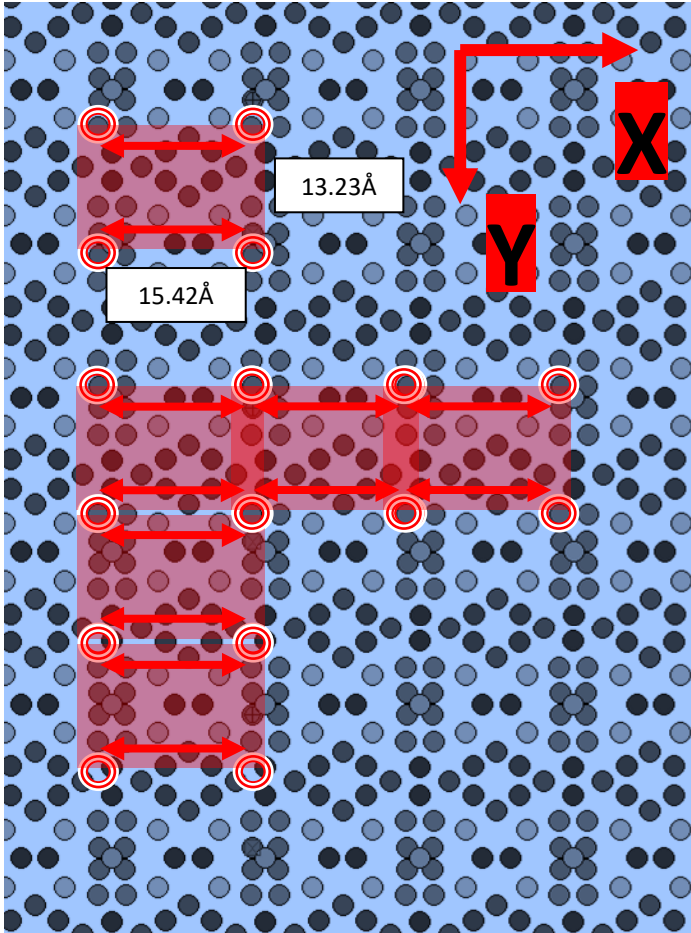


Figure 34: On the A/A' plane a rectangle with the lengths shown in the diagram can fit in between cluster cores. However its shortest length (13.23Å) makes it impossible for it to tile in the Y axis: note that the red circles never land directly on atomic positions when translating in Y after the first tile. When translating in X however they do tessellate.

It can be proven geometrically however that any attempt to tile with a rectangle in such a 2-fold system arranged on a square lattice cannot be achieved without a change in the atomic structure. I.e. Figure 34 shows consecutive tilings of the 0.882 scale rectangle: newly added tiles will never intersect with the model, for the averaged scaling factor is irrational. This can be confirmed through calculation of how many times the difference between the periodic lattice constant a and the rectangular width a_y can fit into a :

$$\frac{a}{a - a_y} \in Z$$

where Z is any irrational number. In the x direction the tiles can repeat periodically along the model surface.

One interpretation of this conundrum is that the surface undergoes extensive reconstruction so that the whole surface lattice is shifted. This however does not correlate with the LEED data obtained from the two separate approximant samples and has little credibility when stacked up against corresponding literature. The possibility of thermal drift or miscalibration unlikely due to the recurring phenomena being observed in the majority of STM images all at

different image tilts (including those not included in the data set). The observed rectangular structures could be explainable within the pending ridged model adaptation currently being researched by Krajčí et al, but only if the B/C planes are involved.

Not all of the cluster-resolution STM images showed rectangular lattice symmetry. Two of the twelve selected images possessed an average square lattice cluster spacing of $a = 15.1\text{\AA}$. The Shimoda model infers that we'd expect to find square symmetries from both the A/A' and B/C planes, but in the absence of high-quality proximity groups the possibility of either A/A' or B/C possessing rectangular symmetry as well as a square lattice cannot be determined with certainty.

Observing steps and cluster resolution within the same image is the only other way of distinguishing terraces from each other so that A and A' are known and B and C are known.

5.5.3. CLUSTER RESOLUTION OF TERRACE STEPS

Of all the data, only one image caught a glimpse of the terrace step heights and the atomic clusters situated in the terraces.

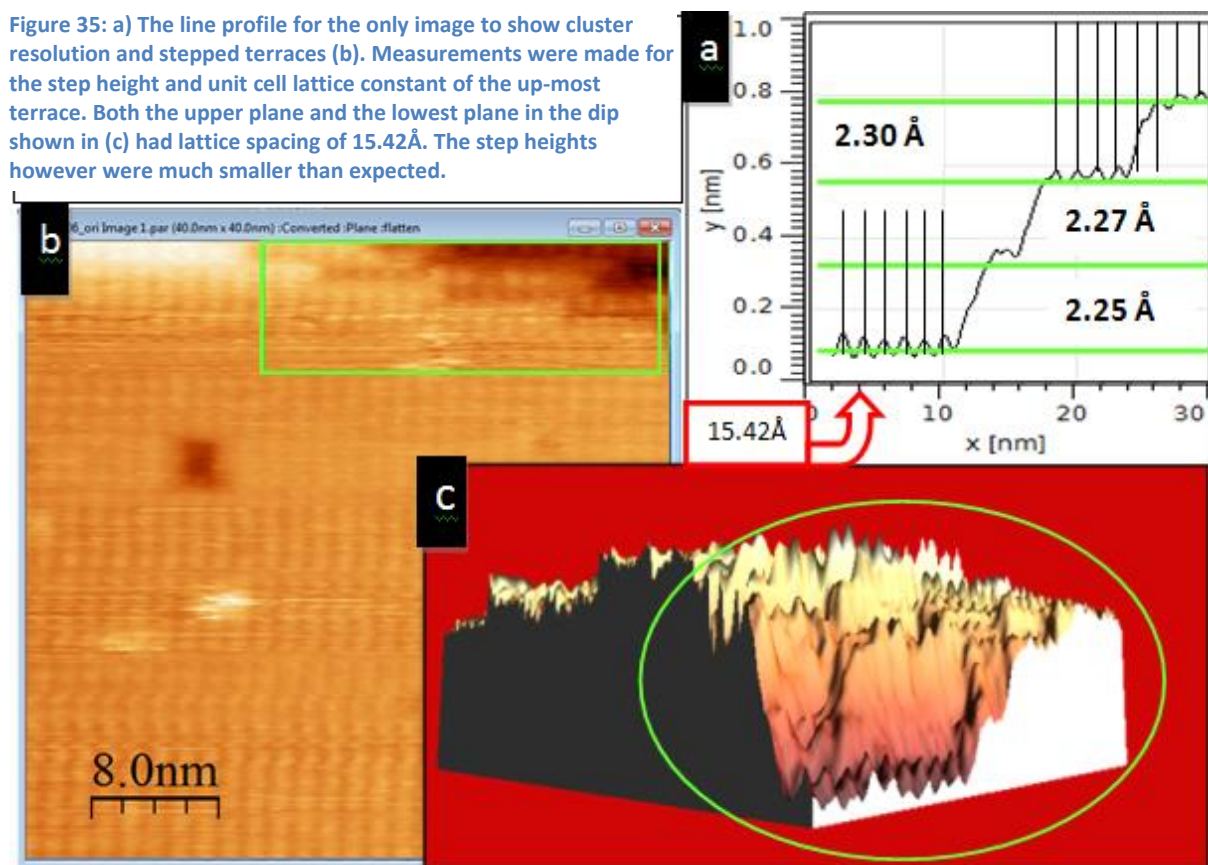


Figure 35.b) isn't convincing to look at, at first. However, the top right hand corner of the image revealed step heights as seen in Figure 35.a) and c). The difficulty in measuring the step-height was overcome with the use of heavy filtering, which appears to have distorted the step height values. The square lattice structure contained unit cell vectors close to $a = 15.42\text{\AA}$, however it is not known which of top and bottom terraces resemble the A/A' planes.

The step heights measured suggest that the intermediate planes are not present and are replaced by lesser planes. The search for better resolution images and a greater proportion of the step in the scope of the STM tip by the STM experimenter was fruitless. Confirmation of square lattice parameters in the A/A' terraces would have deduced that the rectangular unit cells are almost certainly embedded in the intermediate (or perhaps lesser) planes.

5.5.4. ATOMIC RESOLUTION

Attaining good atomic resolution is often reserved for low temperature STMs, where thermal fluctuations and mechanical vibrations are dampened to near-nothingness. It was with some surprise that areas of some of the images contain bands of what at first looked like noise, but turned out to be glimpses of atoms. Internal atomic structures rarely appeared, but in Figure 36 the atoms show up as rectangles of dots nestled in the dark pit regions. (highlighted blue) Heavy filtering of FFT produced a phase pattern (black and white) which was laid over the filtered data (green) and the contrasting 'atoms' were discovered.

The average distance between the blue dots (green arrows) in the relative x direction was measured as 13.22\AA , while in the relative y direction it was measured as 15.40\AA . This is very close to the small length of the rectangles found in A/A'; planes as suggested in the cluster spacing results. Experimentally the atomic resolution images provides just enough information to predict that the terrace is of A/A' origin. However the atomic resolution data has no step height information to compare to: this would be the next stage of analysis had a



Figure 37: the green arrows highlight contrasting bumps in the FFT overlaid pattern: the size and occurrence of these dots seems likely to suggest atomic formation of rectangles.

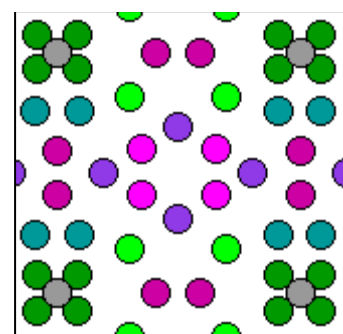


Figure 36: Off centre rectangular unit cell of the A/A' planes: possibly discovered in the atomic resolution data.

functioning STM system been available.

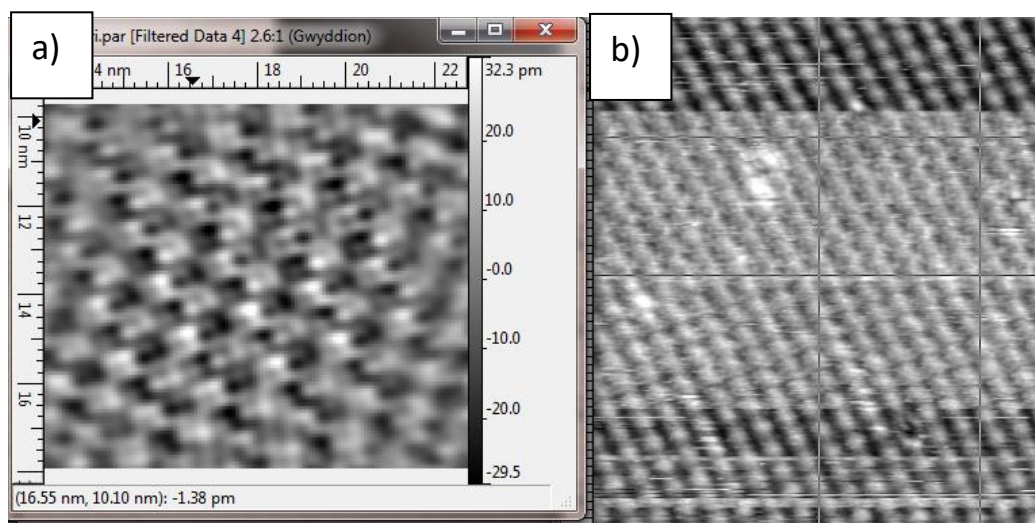


Figure 38: a) FFT phase pattern of a cropped region in b) where b) is the same image as used in Fig.36.

Figure 38 shows the operation of another FFT filter that extracts a different phase pattern from the same image. This pattern appears more angled, and the small holes between the more intense ‘boxes’ appear to represent gaps in the terrace where fewer atoms are present. The high density A/A’ planes have many atoms spread across them, however in the cross over regions between cluster cores there are less, forming a doughnut shape. (see Figure 37) The A/A’ planes could offer the necessary rectangular unit cell with some change to the inherently 2-fold structure of the planes. What should be noted is that the start and end points of the rectangular unit cell in A/A’ lie on the inner most shell of the Tsai cluster. The tetrahedron used in the model is actually an under-populated icosahedron, and the exact positions of the atoms in this shell are unknown: it is expected that herein lays an explanation for the repeating rectangular unit cell.

If it were more likely that the B/C plane was being imaged, then perhaps the ridged terrace could explain the existence of intense boxes – exposed Yb icosahedral clusters forming the peaks in the ridges – however the B/C plane does not have the correct sized rectangular geometries in the model to match the data. The length of the rectangular unit cell in B/A is $a_y = 12.83\text{\AA}$, and this has not occurred in the data set.

5.5.5. SUMMARY

- STM images with scan areas smaller than 200 x 200nm provided cluster separation distances which were measured by line profiling.
- Deviations from the predicted (100) square lattice of $a = 15.42\text{\AA}$ were observed in the majority of measurements made on the data set of twelve images.
- The lattice vectors measured were found to be related by ratio of $a_x:a_y$ which was found in the Shimoda model in an off-centre rectangle in the A/A' planes.
- *Model rectangle ratio in A/A' planes* $a_x:a_y = 13.60\text{\AA} : 15.42\text{\AA} = 0.882$
- *Measured (average) ratio in A/A' planes* $a_x:a_y = 13.23\text{\AA} : 15.41\text{\AA} = 0.858$
- *Model rectangle ratio in B/C' planes* $a_x:a_y = 12.83\text{\AA} : 15.41\text{\AA} = 0.832$
- The A/A' ratio was consistently closer than the B/C ratio to the measured ratio.
- With the high frequency of the A/A' plane ratio occurring in the data set, an assumption was made that the majority of planes imaged were stable A/A' planes. (assumption made in the absence of good quality proximity groups to test theory)
- Drift and other systematic errors are ruled out due to the consistency of results...
- ...although the presence of some square lattice separations presents a challenge in defining what tilings are allowed on different density planes.
- An unknown influence from the Indium-decorated tetrahedra (at the centre of the Tsai clusters) on the creation of the rectangular unit cell is proposed as a solution to the geometric problem of tiling rectangles in the A/A' y-axis.
- Atomic positions on the corners of a rectangle of aspect ratio $a_x:a_y = 0.858$ are observed, a strong indication of A/A' plane presence.
- Doughnut shaped holes in the FFT phase pattern suggest atomically vacant zones that could belong to either the A/A' or B/C planes.
- Ultimately, higher resolution images of terrace stepping with cluster-level or greater detail are required to confidently characterise the terraces.

6. CONCLUSION AND FURTHER RESEARCH

The approximant Ag-In-Yb project presented its fair share of challenges to overcome. Without the use of a suitable sample to calibrate the LEED apparatus, a compensation method was used with Cu(111): a scaling factor of the sine of the angle of diffraction was found to behave as $1/\sqrt{E}$, which meant halving E would change the angle by $\sin^{-1}(\sqrt{2})$. The angle at which the Cu LEED pattern for 65eV was found was $\theta_f = 45.9^\circ$. This was scaled to $\theta_f = 76.6^\circ$ when the energy was halved. To acquire these values, knowledge of the (111) surface and the diffraction directions was imperative. This allowed for the measurement of the Ag-In-Yb reciprocal lattice vectors which turned out to be 13% smaller than the predicted value of $a = 15.42 \text{ \AA}$. This was consistent with the simplicity of the approach, and served to illustrate the effect of electron beam energy on the diffraction angle. Taking LEED analysis further, detailed structural analysis using I-V LEED to examine the intensity and phase of diffraction spots should be considered to complement future STM investigations.

The problems with the STM vibrational isolation valve had a huge impact on the whole project, resulting in the use of STM images of Ag-In-Yb taken using a similar system but with very few indicators of the process by which they were taken. Of the 115 images, very few were suitable, however indexing the data using proximity groups made it very easy to return to groups of images and explore relative images in a pan/zoom fashion similar to the process of obtaining the STM data. This resulted in many more suitable images being found and atomic resolution being hinted at in the best case scenario. Measurement of step heights was accomplished with relative ease thanks to the set of tools provided by *Gwyddion* and *WSxM*. After suitable filtering, the implementation of the height-histogram method saved enormous amounts of time and energy: it could be applied to whole images or cropped areas instead of having to be manually positioned over terrace steps. *Graph 1* indicated that stable planes exist not just in the high density A/A' planes, but also in the intermediate B/C planes, and the qualitative assessment of the small data set made it clear that future experiments need to focus on acquiring data from large terraces as they will be the most stable and will relate to A/A'/B/C planes.

Line profiling and FFT filtering were specially used to investigate the separation of Tsai clusters: the results of the STM analysis were very thought provoking. Rectangular tiling in the A/A' planes cannot exist in the Shimoda model, however this very geometry is observed at atomic resolutions. The rectangular ratio of lengths was measured as: The rectangle unit is

based upon Indium atoms in the very centre of the Tsai cluster. This under-populated region differs in density between different approximants (1/1, 2/1 etc) and further study into the affect of exposing the A/A' planes will most likely include a reappraisal of the Tsai cluster structure.

It is hoped that the most recent proposal for model modification (Krajčí et al) will provide an insight into predicted ridged B/C planes. It is believed that no quantifiable examples of the ridged structures were observable in the data set, but this does not mean they were not present. Chance determined that atomic resolution was obtained for the A/A' terrace instead of the B/C planes, so experimenters will have a vested interest in pioneering the first observation of this ridged structure.

Very few other improvements could have been made to the project when accounting for time restrictions. A study of epitaxial growth of Pb / Bi to compare with layer growth on the *i*-Ag-In-Yb QC will ultimately be of the most benefit to the Surface Science Department: as the international surface science community continues to search enthusiastically for clues as to the affect of quasiperiodicity on metal properties, such surface studies will be vital in the race to discover new quasicrystal related phenomena.

Bibliography

- Attard, G. & Barnes, C., (1998) “*Surfaces.*” Oxford Uni. Press Issue 59, Ox. Chem. Primers.
- Bindi, L., Steinhard, P. J., Yao, N. & Lu, P. J., (2011) “*Icosahedrite, Al₆₃Cu₂₄Fe₁₃, the first natural quasicrystal.*” *American Mineralogist* 96, 928-931.
- Dubois, J., (2002) “*Useful Quasicrystals.*” World Scientific Publishing Co.
- Franke, K. J. & Berlin, F. U., (2003) “*Quasicrystal Surfaces: Morphology, Phase Transitions, and Epitaxy.*” Available at: [doi: FUDISS derivate 000000001461](https://doi.org/10.1007/978-1-4020-0000-0_1461) [Accessed Apr-12].
- Gomez, C. P., (2003) “*Order and Disorder in the RE-Cd and Related Systems*” 54–64 Stockholm Uni.
- Krajčí, M. & Sharma, H.R. (2012) *Private Correspondence.*
- Meier, W., (1984) “*14 - Space Group Patterns,*” International Union of Crystallography.
- Nugent, P. et al., (2010) “*Surface oxidation of the icosahedral Ag-In-Yb quasicrystal.*” *Phys. Rev. B* 82
- Nugent, P. et al., (2011) “*Step-terrace morphology and reactivity to C₆₀ of the five-fold icosahedral Ag-In-Yb quasicrystal.*” *Philos. Mag.* 91, 19.
- (2003) “*SpectraLEED Optics and Electron Source.*” Omicron NanoTechnology
- Owens, R., (1997) “*Fourier transform theory.*” Available at: http://homepages.inf.ed.ac.uk/rbf/CVonline/LOCAL_COPIES/OWENS/LECT4/node2.html [Accessed 2012].
- R.Noorden, N. N., (2011) “*Impossible crystals snag chemistry Nobel.*” Available at: [doi: 10.1038/news.2011.572](https://doi.org/10.1038/news.2011.572) [Accessed Mar-12].
- Ritsch, S. & Nissen, H.-U., (1996) “*Phason related stacking disorder in decagonal Al-Co-Ni.*” *Phys. Rev. Lett.* 76, 2507.
- Sharma, H. R., (2011) “*Surface Physics: Electron Diffraction*” PHYS381 Uni. Liverpool. Lecture Series.
- Sharma, H. R., Shimoda, M., Smerdon, J. A. & Tsai, A. P. (2009) “*Structure of the fivefold surface of the Ag-In-Yb icosahedral quasicrystal.*” *Phys. Rev. B* 80.

Sharma, H. R. et al., (2010) “*Valence band structure of the icosahedral Ag-In-Yb quasicrystal*” Phys. Rev. B 81.

Shechtman, D., Blech, I., Cahn, D. & Gratias, J., (1984) “*Metallic Phase with Long-Range Orientational Order and No Translational Symmetry*” Phys. Rev. Lett 20, 53.

Shimoda, M. & Gomez, C. P., (2011) *Private Correspondence*.

Stadnik, Z. M., (1999) “*Physical Properties of Quasicrystals.*” Springer Sol. St. Sci. 126.

Takakura, H. et al., (2007) “*Atomic structure of the binary icosahedral Yb–Cd quasicrystal.*” Nature Mater. 6, 58.

Tsai, A. P., (2009) “*Growth of large single-grain quasicrystals in the Ag–In–Yb system by Bridgman method.*” Jour. Cryst. Grow.

Zallen, R., (1998) “*The Physics of Amorphous Solid.*”. Wiley Interscience.

APPENDIX I: SAMPLE PREPARATION

POLISHING A CRYSTAL SAMPLE

The sputtering and annealing cycle requires that the sample is already cut perpendicular to a desired axis and is subsequently polished. Before UHV treatment, the sample is polished using high-quality diamond-grain paste and rough/fine polishing paper. To reach the level of flatness required for diffraction investigation or STM, several grades of polish paste are used, progressively reducing in grain size from (first) $6\mu\text{m}$ -grade, then to $1\mu\text{m}$, then finally $0.25\mu\text{m}$. The highest grade ($6\mu\text{m}$ paste) requires a roughened quality of polish paper to strip away the majority of scratches and defects. Later grades tidy up the surface through softening of hidden edges and use a finer quality paper. By rotating and/or tilting the sample using tweezers and training a lamp on the surface the light will be able to pick up on grooves or irregularities. However small these defects appear, a perfectly polished sample should have none visible to the naked eye: the closer to this standard, the more successful the experiment will be. In order to be confident in the surface's conformity, an ordinary optical microscope can be used to examine the surface.



Figure 39: Photograph of 1/1 Ag-In-Yb approximant sample on sample plate: the flat shiny side facing up is the (100) plane.

As a rule of thumb the polish paper can be cut down to no wider than three fingers' width. Once the paper is secured in some way to the stage, the paste is applied to the paper in an amount proportional to the size of the sample (usually no more than a deposition of 3mm diameter). Taking care to spread the paste evenly across the paper, the sample is then placed surface-down. Focus even pressure on the sample's reverse side using either one finger, or by carefully pinching the reverse edges. Many different methods of polishing the sample by hand exist, all with the same intention of removing scratches and surface irregularities from the surface of interest through a uniform application of pressure and buffing. The technique used in the investigation of the Ag-In-Yb approximant, as recommended by Sharma *et al* of the UoL Surface Science Dept, was to guide the sample in a clockwise figure of eight for 50 full laps, (or for $2\frac{1}{2}$ minutes) and then repeat in the anticlockwise direction. This 'buffing' treatment of the sample will have to be repeated *with the same polish* until:

- a) (*when using $6\mu\text{m}$ -grade polish*) any deep surface indentations (on the order of mm) are removed and the sample is shiny.
- b) (*$1\mu\text{m}$*) the surface appears completely smooth and shiny under scrutiny by eye.

- c) ($0.25\mu\text{m}$) the surface appears completely smooth and shiny under the scrutiny of an optical microscope.

Note that the pressure exerted on the sample should be relaxed as nearing the end of a polishing cycle: polishing lightly guarantees that all the previous effort of polishing does not accidentally cause new scratches to appear from contaminating particles.

The polishing setup should observe standard anti-contamination procedures: throughout this project methanol and perforated blue tissue are used to sterilize an aluminium slab to use as a work stage, as well as the surrounding work area. After buffing, the sample should always be rinsed with methanol. Used polishing paper should immediately be discarded if the residue coming from the sample thickly coats the paper. Any residue remaining on gloves should be washed off using methanol. Very importantly, the sample should always be placed in a sonic water bath when changing from grade to vigorously remove unwanted particles deposited on the surface during polishing. A 15 minute bath in methanol is sufficient to keep the surface clean during polishing; however when the polishing and mounting process is finished it is advisable to bathe the sample with two 15 minute cycles, each in a fresh solution of methanol.

MOUNTING THE SAMPLE

There are many approaches to fix a sample to a plate for transfer into an UHV environment. Mounting epoxies have been developed that can withstand intense annealing temperatures (more than 600°C , or a heat-resistant cage can be welded to the plate over the crystal sample. As the sample requires being able to be rotated in the chamber, the more proven and less risky method of cage mounting is used in this report.

First, the sample plate should have its faces filed down using a fine-crosshatched) file, the aim being to erase abrasions or relics of previous mounting and to gently reveal un-oxidised layers of the plate. The surface is then rinsed with methanol, as is the sample, and placed in the centre of the plate

Wire- or foil-cage mounting is much safer than using an epoxy, mainly because the epoxy's integrity cannot be guaranteed until it has reached the temperature its manufacturer claims it can withstand. The upper boundary temperatures used in annealing copper, 675°C and for the annealing of Ag-In-Yb (420°C ~ an estimated value projected from the quasicrystal sample

optimum annealing temperature) rule out any easily acquirable / affordable epoxies. Alternatively, a cage can be put under small tensile forces to test the welding strength. Also, multiple contact sites with the sample plate reduces the likelihood that the sample could fall off (a potential disaster for the experimenter who must then open up the chamber to air in order to retrieve the lost sample!). Oxidation of the plate or cage during welding can be a source of sample contamination; however as mentioned in the last section we can counteract this using the sonic bath. More thoroughly:

- a) A Tungsten Wire Cage – tungsten has the highest melting point of all non-alloy metals, making it an ideal candidate for the cage. It has a noticeably robust nature, yet tungsten wire of 0.25 mm diameter is flexible enough to conform to the shape of the sample when bent. Other *pro* qualities include: thin wire can be welded using a spot-welder; thin wire obstructs very little of the sample, even when using more than two wires, allowing for greater sampling range in both LEED and STM experiments; thin wire can readily conform to irregular sample shapes; the cage can be reused multiple times with different samples of similar shape; easy to remove off of plate when finished with. *Cons*: the wire is difficult to return to a straight form; irregular samples require more pieces of wire.
- b) A Tantalum Cage – tantalum is a highly inert material that is adept at resisting heat, however in a wire form can be quite brittle when bent more than once in the same place. Its foil form is more ductile, and use of foil of thicknesses 0.25mm has been shown to secure samples in two different ways. The first is similar to that of the tungsten cage where we replace the wires with tantalum bands only a few mm wide. The other is to take the thinner dimension of tantalum, cut a cross into a foil square larger than the sample (keeping 5mm away from the edge of the plate) then carefully presses the sample through the vacancy in the foil. Spot-welding around the sample-perimeter forces triangular walls up against the crystal, holding it successfully in place. *Pros*: tantalum can be readily used as a substitute for tungsten wire; foil is flexible enough to reshape; can form a very tight cut-cage with some careful design; band cage usually only needs two strips. *Cons*: welding has a tendency to take several attempts that can heavily oxidise the plate contact site; cut-cage not suitable for irregular shapes; when removing flimsy foil remnants, extra care and persistence is needed so not to scratch the plate.

The spotwelder used for welding the cage has several useful built-in features. The welder electrode contacts are designed to weld very small areas via the heat obtained from resistance to electrical current. The contacts have a vice-like grip that presses the wire against the plate and forms a conductive channel. Control over the current flow is overseen by a power supply, which can not only increase the welding heat but also vary the frequency of welding cycles when triggering the welder. Furthermore, there are two stages required to trigger the welder: an appropriate exertion of pressure when clamping the electrodes down (a click confirms the trigger is primed), and a floor-paddle. This allows the experimenter to alter the position of the wire / foil using the contacts themselves before triggering the flow of current (as opposed to requiring the user to get it right the first time). The weld time is of the order of milliseconds, though depending on power supply settings and shape of the wire several welds may be needed for a secure fix.

A clean stage and clean equipment are essential, and moving the sample is best done with tweezers. Never use the contacts to move the sample, and don't weld if the contacts are in direct contact with for this can both contaminate and melt the crystal. The contacts and the cage material should be cleaned with methanol and blue tissue. The RT-STM chamber manipulator accepts plates of approximately 22mm x 18mm x 1.5mm dimensions. For the plate to be transferred into the manipulator there needs to be an area around the edge of the plate that is completely flat; be aware that the contour of the cage/sample will prevent the plate from slotting into the manipulator clips if it comes within 4mm of the edge.

Both the tantalum and tungsten are welded by the same method; we refer from now on to 'wire' to denote that tungsten was the material chosen in this investigation.

First the sample is orientated with its polished

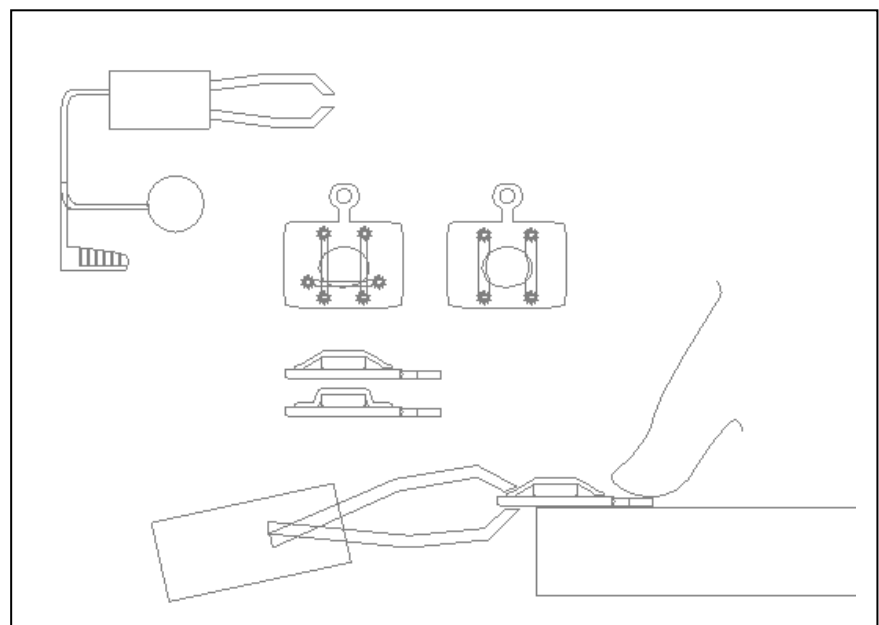


Figure 40: a) Diagram showing the spot welder, with floor pedal and dial control. b) Wire cage mounting. c) Tantalum band mounting. d) The preferred mounting, in which the cage applies as much force as possible by being stretched taut. e) In this picture, the sample is shown in a less desirable cage, and it may move or fall out during experimentation. f) Placing the thumb on the plate whilst welding.

surface facing up in the centre of the plate. Lengths of wire are made to manageable sizes that extend longer than the plate dimensions; the wire can be cut shorter after welding. The wires are then laid in a pattern suited to the shape and size of the sample, as shown in figure **B**. An easy way to begin is then to select just one of the wires, remove the others from the sample, and then (whilst holding the sample steady with tweezers) use the electrodes to clamp down on one end of the wire. Triggering the spot-welder will often produce sparks from the resistance heating and is a good sign that the welding is forming a metallic bond. Once the wire is fixed, it is bent over the sample and welded on the other side. With the sample now held in by one wire, the remaining wires can be added. Keeping the wire taut over the sample (case d) is preferable to bending the wire to a snug fit (case e) : this is because the crystal mustn't be 'supported' by the cage, for this gives it too much freedom of movement. It must be restrained through the application of perpendicular force.

An irregularly grown crystal can cause much misery to the experimenter (or postgraduate!) when mounting. More opportunities arise for displacement of the sample when its sides are multifaceted, especially when the crystal is not secured with taut wire (see next chapter for solutions to this problem). Prevention is better than the cure – especially when the prospect of removing the whole cage to start again looms overhead – so throughout spot-welding one should nudge the sample to see if it is being kept from rotating or sliding about the plate.

SPUTTERING AND ANNEALING

Once the sample is polished, mounted and cleaned using the sonic bath, the sample can finally enter the chamber and undergo sputtering and annealing. This stage of the preparation of a sample is crucial as polishing alone cannot obtain atomically smooth terraces. We can assume that the Ag-In-Yb approximant sample will behave similarly to its QC counterpart: the change in surface composition upon sputtering and annealing was previously analyzed for the fivefold surface. It was found that In and Yb are preferentially removed from the surface resulting in Ag enrichment in the surface region. Sputtering in the UHV chamber uses Ar^+ at pressures of 3×10^{-5} mbar; ion pumps must be turned off to prevent damage of the ion filaments. Annealing at temperatures between 420-430°C restores surface composition close to the bulk. This is done through diffusion towards the surface of the sample. After annealing, the surface displays terraces and steps of different heights which can be investigated by STM.

APPENDIX II: STUDENT FEEDBACK AND THANKS

Surface science has always been the scientific field of the greatest interest to me, ever since being introduced to the “nano-age” through science fiction and then subsequently through studying Physics at university level. The experimental nature of this project appealed to me greatly, and a lot of the experience I gained was through a collaborative process involving many of the members of the department. I found it most encouraging that the group was well integrated and that progress on one research front always benefited another in some way; whether it was through the acquisition of new knowledge, or via the cooperation of a third party.

During the last semester Joe Smerdon arranged a series of group meetings that I benefited greatly from. I was forced to turn down a chance to give a presentation at the group talks, which would have been very practical experience to obtain. I would recommend more of this kind of involvement between Masters students and the research group at large.

My only complaint would be that the software used in image analysis required intuitive and experienced guidance to extract meaningful data, and I certainly would have preferred to have started using it at the very beginning of the dissertation in order to save time later on. Otherwise, my volunteer work over the summer of 2011 provided me with many of the skills I would need through the dissertation.

My utmost appreciation and gratitude goes to the following members of the Surface Science Department of the University of Liverpool:

H.R. Sharma, J. Smerdon, T. Yadav, S. Hars, K. Young, S. Haq, and M. Lowe.

A special mention also goes to Visiting Professor R. Tamura from Tokyo University of Science for his advice and generosity during his stay with the department.

~Kai McGilligan Oliver

